

Constraining Non-Standard Interactions with Coherent Elastic Neutrino-Nucleus Scattering at the European Spallation Source

Sabya Sachi Chatterjee,^{1,*} Stéphane Lavignac,^{1,†} O. G. Miranda,^{2,‡} and G. Sanchez Garcia^{2,3,§}

¹*Institut de Physique Théorique, Université Paris Saclay, CNRS, CEA, F-91191 Gif-sur-Yvette, France*

²*Departamento de Física, Centro de Investigación y de Estudios Avanzados del IPN, Apartado Postal 14-740 07000, Ciudad de Mexico, Mexico*

³*Instituto de Física Corpuscular (CSIC-Universitat de València), Parc Científic UV, C/ Catedrático José Beltrán, 2, 46980 Paterna, Spain*

The European Spallation Source (ESS), currently under construction in Sweden, will provide an intense pulsed neutrino flux allowing for high-statistics measurements of coherent elastic neutrino-nucleus scattering (CE ν NS) with advanced nuclear recoil detectors. In this paper, we investigate in detail the possibility of constraining non-standard neutrino interactions (NSIs) through such precision CE ν NS measurements at the ESS, considering the different proposed detection technologies, either alone or in combination. We first study the sensitivity to neutral-current NSI parameters that each detector can reach in 3 years of data taking. We then show that operating two detectors simultaneously can significantly improve the expected sensitivity on flavor-diagonal NSI parameters. Combining the results of two detectors turns out to be even more useful when two NSI parameters are assumed to be nonvanishing at a time. In this case, suitably chosen detector combinations can reduce the degeneracies between some pairs of NSI parameters to a small region of the parameter space.

I. INTRODUCTION

Coherent elastic neutrino-nucleus scattering (CE ν NS) was predicted by Freedman more than forty years ago [1]. In this process, the neutrino interacts with the whole nucleus through the exchange of a virtual Z boson. For this to happen, the transferred momentum should be comparable with the inverse of the nucleus radius or smaller. The contributions of the individual nucleons then add coherently, resulting in a cross-section that approximately scales like the squared number of neutrons in the target nucleus, thus making CE ν NS dominant over other neutrino interactions, such as neutrino-electron scattering. Since the process is elastic, its only effect is to redistribute the kinetic energy between the neutrino and the nucleus. Therefore, its detection requires the measurement of the recoil energy acquired by the nucleus. The smallness of the typical recoil energies made the CE ν NS observation a challenging task for decades. It was only in 2017 that the COHERENT collaboration [2] reported the first measurement of CE ν NS [3], using a CsI [Na]-based detector and neutrinos produced from the Spallation Neutron Source (SNS) at Oak Ridge National

* sabya-sachi.chatterjee@ipht.fr

† stephane.lavignac@ipht.fr

‡ omar.miranda@cinvestav.mx

§ gsanchez@fis.cinvestav.mx

Laboratory. In the following years, the collaboration reported a second measurement in a LAr detector [4], and another data set from the CsI measurement was released [5].

The COHERENT data has been used by several authors to perform tests of the Standard Model (SM) and to constrain its possible extensions. As a probe of standard physics, $\text{CE}\nu\text{NS}$ is sensitive to the value of the weak mixing angle at low energy [6–10] and to nuclear parameters such as the neutron *rms* radius [8, 11–13], which is well known only for a few elements. As for physics beyond the SM, the COHERENT data has been used to constrain non-standard interactions (NSIs) of neutrinos [9, 14–20], generalized neutrino interactions [21–24], light mediators [25–31], massive scalar and vector mediators [32, 33], sterile neutrinos [21, 34–37], non-unitarity of the lepton mixing matrix [36], and neutrino electromagnetic properties such as the neutrino charge [8, 38] and magnetic dipole moments [38, 39]. The precise measurement of the $\text{CE}\nu\text{NS}$ cross-section has applications in other fields, such as direct dark matter detection, where it is important for estimating the so-called neutrino floor [40]. There is also an interest in using $\text{CE}\nu\text{NS}$ for nuclear security and monitoring purposes [41].

Significant progress has been made in the characterization of detection materials for $\text{CE}\nu\text{NS}$, and several experimental programs aim at measuring $\text{CE}\nu\text{NS}$ with neutrinos produced at spallation neutron sources in the coming years. For instance, the complete program of the COHERENT collaboration considers Ge and NaI detectors [2]. Other experiments like the Coherent Captain Mills detector at Los Alamos National Laboratory will use LAr as target material [42]. Another interesting proposal is to perform high-statistics $\text{CE}\nu\text{NS}$ measurements at the upcoming European Spallation Source (ESS) [43]. Other experiments aim to measure $\text{CE}\nu\text{NS}$ with reactor neutrinos, such as CONUS [44], CONNIE [45], NUCLEUS [46] and RICOCHET [47].

The European Spallation Source (ESS), currently under construction in Lund, Sweden, will provide the world’s most intense neutron beams, allowing for a rich experimental program. As a by-product, it will yield a large pulsed neutrino flux suitable for high-statistics measurements of coherent elastic neutrino-nucleus scattering ($\text{CE}\nu\text{NS}$), for which six different advanced detection technologies have been proposed in Ref. [43], namely CsI, Ge, Ar, Si, Xe and C_3F_8 based detectors. The possibility to probe NSIs through $\text{CE}\nu\text{NS}$ measurements at the ESS was considered for the first time in the same paper [43], where the 90% C.L. expected sensitivity to the flavor-diagonal non-standard neutrino couplings to the up quark was computed for the six above-mentioned detectors. It was also shown that combining the data of a gas time projection chamber (TPC) detector filled alternatively with Xe and Ar would significantly reduce the degeneracy between the same two NSI parameters.

In this paper, we investigate in greater detail the capability of $\text{CE}\nu\text{NS}$ measurements at the ESS to constrain non-standard neutrino interactions. We present the expected sensitivities of each of the six detectors proposed in Ref. [43] to all relevant NSI parameters, considered one at a time or in pairs, and quantify the improvement that can be obtained by combining the data from two detectors. We also compare the capabilities of different detector combinations to break the degeneracies that appear when two NSI parameters are assumed to be simultaneously nonvanishing, and identify the most efficient ones for that purpose.

The paper is structured as follows: in Section II, we give the cross-section for $\text{CE}\nu\text{NS}$ both

within the SM and in the presence of NSIs. In Section III, we present the experimental setup of the ESS, and we describe the procedure that we follow to study the expected sensitivities of the different proposed detectors to NSI parameters. We present our results in Section IV, and give our conclusions in Section V.

II. THEORETICAL FRAMEWORK

At a spallation neutron source like the ESS, high-energy protons hit a fixed mercury target, producing neutrons and charged pions. The π^- are absorbed by the nuclei of the target, whereas the π^+ lose their energy and decay at rest as $\pi^+ \rightarrow \mu^+ + \nu_\mu$. The muon neutrinos arising from this decay are monochromatic and are called *prompt neutrinos*. The positively charged muons produced along with the muon neutrinos decay in turn at rest, producing two additional neutrinos, $\bar{\nu}_\mu$ and ν_e , called *delayed neutrinos*. The total neutrino flux is therefore the sum of three components:

$$\frac{dN_{\nu_\mu}}{dE_\nu} = \xi \delta \left(E_\nu - \frac{m_{\pi^+}^2 - m_\mu^2}{2m_{\pi^+}} \right), \quad (1)$$

$$\frac{dN_{\bar{\nu}_\mu}}{dE_\nu} = \xi \frac{64 E_\nu^2}{m_\mu^3} \left(\frac{3}{4} - \frac{E_\nu}{m_\mu} \right), \quad (2)$$

$$\frac{dN_{\nu_e}}{dE_\nu} = \xi \frac{192 E_\nu^2}{m_\mu^3} \left(\frac{1}{2} - \frac{E_\nu}{m_\mu} \right), \quad (3)$$

where E_ν is the incoming neutrino energy (with $E_\nu \leq m_\mu/2 \simeq 52.8$ MeV for the $\bar{\nu}_\mu$ and ν_e neutrinos) and $\xi = rN_{\text{POT}}/4\pi L^2$, in which $r = 0.3$ is the number of neutrinos of each flavor produced by a single proton on target, N_{POT} is the total number of protons on target (POT) and L is the distance from the source to the detector (with $N_{\text{POT}} = 2.8 \times 10^{23}$ per calendar year and $L = 20$ m at the ESS).

After traveling a distance L , neutrinos are detected through their coherent elastic scattering off the target nuclei. At tree level, in the SM, the differential cross-section for this process is independent of the flavor of the incoming neutrino [48]. For a neutrino (or antineutrino) of energy E_ν scattering off a nucleus with Z protons, N neutrons and mass M , it is given by

$$\frac{d\sigma}{dT}(E_\nu, T) = \frac{G_F^2 M}{\pi} \left(1 - \frac{MT}{2E_\nu^2} \right) F(|\vec{q}|^2) (Q_W^V)^2, \quad (4)$$

where G_F is the Fermi constant, T the recoil energy of the nucleus and $F(|\vec{q}|^2)$ the nuclear form factor (assumed to be the same for neutrons and protons) evaluated at the transferred three-momentum, $|\vec{q}| \simeq \sqrt{2MT}$. The weak nuclear charge Q_W^V reads, in the SM,

$$(Q_{W,\text{SM}}^V)^2 = (Z g_V^p + N g_V^n)^2, \quad (5)$$

where $g_V^p = \frac{1}{2} - 2 \sin^2 \theta_W$ and $g_V^n = -\frac{1}{2}$ are the neutral current vector couplings¹. In our calculation, the weak mixing angle is taken at zero momentum transfer ($\sin^2 \theta_W = 0.23867$ [49, 50]), as the

¹ The contribution of axial couplings is proportional to the nucleus spin and is expected to be suppressed, with respect to the contributions of the vector couplings, by a factor $1/A$, where A is the number of nucleons.

transferred three-momentum is constrained to be very small by the coherence condition (typically a few tens of MeV). Throughout this work, we use the Helm parametrization [51] for the nucleus form factor²:

$$F(|\vec{q}|^2) = 3 \frac{j_1(|\vec{q}|R_0)}{|\vec{q}|R_0} e^{-|\vec{q}|^2 s^2/2}, \quad (6)$$

where j_1 denotes the spherical Bessel function of order one, $s = 0.9$ fm [55] is the surface thickness and $R_0^2 = 5/3 (R^2 - 3s^2)$, with R the neutron rms radius.

Let us now discuss how CE ν NS is affected by the presence of non-standard neutrino interactions (NSIs). NSIs, whose impact on neutrino propagation in matter was first discussed in Ref. [56], are a possible low-energy manifestation of new physics in the lepton sector. They are usually parametrized in terms of higher-dimensional operators in the effective field theory of the SM below the weak scale. As a neutral current process, CE ν NS is only affected by neutral current NSIs (NC-NSIs), which are described by

$$\mathcal{L}_{\text{NC-NSI}} = -2\sqrt{2} G_F \varepsilon_{\alpha\beta}^{fC} (\bar{\nu}_\alpha \gamma^\mu P_L \nu_\beta) (\bar{f} \gamma_\mu P_C f), \quad (7)$$

where $\alpha, \beta = e, \mu, \tau$ denote the neutrino flavors, $f = e, u, d$ label the matter fermions, $C = L, R$ corresponds to the chirality of the matter fermion current, and $\varepsilon_{\alpha\beta}^{fC}$ are the strengths of the NSIs. Hermiticity of the Lagrangian requires $\varepsilon_{\beta\alpha}^{fC} = (\varepsilon_{\alpha\beta}^{fC})^*$. In this work, we will only consider the vector-type³ NC-NSIs

$$\varepsilon_{\alpha\beta}^{qV} \equiv \varepsilon_{\alpha\beta}^{qL} + \varepsilon_{\alpha\beta}^{qR}, \quad q = u, d. \quad (8)$$

Then, for an incident neutrino or antineutrino of flavor α , the weak nuclear charge Q_W^V in Eq. (4) is modified to [14]

$$\begin{aligned} (Q_{W,\alpha}^V)^2 &= [Z (g_V^p + 2\varepsilon_{\alpha\alpha}^{uV} + \varepsilon_{\alpha\alpha}^{dV}) + N (g_V^n + \varepsilon_{\alpha\alpha}^{uV} + 2\varepsilon_{\alpha\alpha}^{dV})]^2 \\ &+ \sum_{\beta \neq \alpha} \left| Z (2\varepsilon_{\alpha\beta}^{uV} + \varepsilon_{\alpha\beta}^{dV}) + N (\varepsilon_{\alpha\beta}^{uV} + 2\varepsilon_{\alpha\beta}^{dV}) \right|^2. \end{aligned} \quad (9)$$

In the next sections, we study the sensitivity to NSIs that the proposed CE ν NS experiments at the ESS can reach. We discuss how the combination of different detectors can help to remove the degeneracies arising when two NSI parameters are assumed to be nonvanishing at a time.

III. EXPERIMENTAL SETUP AND SIMULATION

In this section, we briefly review the experimental specifications of the different detectors proposed for CE ν NS measurements at the ESS. Then we give a detailed description of our simulation procedure.

² For a detailed discussion on the impact of different form factors in CE ν NS the reader can see, for example, Refs. [52–54].

³ NC-NSIs can also have axial components $\varepsilon_{\alpha\beta}^{fA} \equiv \varepsilon_{\alpha\beta}^{fR} - \varepsilon_{\alpha\beta}^{fL}$. However, their effect on CE ν NS is negligible for heavy nuclei [14].

A. Experimental setup options

The European Spallation Source is a highly ambitious and promising multi-disciplinary research facility under completion at Lund, Sweden. It will use a very powerful superconducting proton linac to generate the world's most intense pulsed neutron beams. As a byproduct, it will also generate high-intensity, low-energy neutrino fluxes suitable for the study of coherent elastic neutrino-nucleus scattering (CE ν NS). The ESS will use a proton beam energy of 2 GeV and a beam power of 5 MW, resulting in 2.8×10^{23} protons on target (POT) per calendar year (208 effective days), which will lead to an increase of the neutrino flux by one order of magnitude with respect to the current configuration of the Spallation Neutron Source (SNS) [2] located at Oak Ridge National Laboratory, USA. Furthermore, it is expected that a future upgrade of the proton linac will increase the proton energy to 3.6 GeV. Since the construction of the ESS is underway, it has been proposed to set up a number of different detectors sensitive to very low-energy nuclear recoils, in order to take advantage of the high-intensity neutrino flux to make precision CE ν NS measurements. Following the proposal of Ref. [43], we investigate in this work the physics potential of six different detector targets (CsI, Xe, Ge, Ar, Si, and C₃F₈), alone or in combination.

The differential event rate dN/dT for these detectors is given by the convolution of the ESS flux and the CE ν NS cross-section $d\sigma/dT(E_\nu, T)$ (with the weak nuclear charge given by Eq. (5) in the SM and by Eq. (9) in the presence of NSIs) as a function of the true nuclear recoil energy T :

$$\frac{dN}{dT} = \mathcal{N} \sum_{\nu=\nu_e, \nu_\mu, \bar{\nu}_\mu} \int_{E_{min}(T)}^{E_{max}} dE_\nu \frac{dN_\nu}{dE_\nu}(E_\nu) \frac{d\sigma}{dT}(E_\nu, T), \quad (10)$$

where $\mathcal{N} = N_A M_{\text{det}}/M_{\text{mol}}$ is the number of nuclei in the detector (with N_A the Avogadro constant, M_{det} the detector mass and M_{mol} the molar mass of the detector material), $E_{min}(T) = \sqrt{MT/2}$ (with M the mass of the nucleus) is the minimal neutrino energy required to induce a nuclear recoil energy T , and $E_{max} = 52.8 \text{ MeV}$ is the maximal energy that a neutrino from the ESS flux can have. The maximal value of the nuclear recoil energy is given by $T_{max} = 2E_{max}^2/M$. We assume an experimental running time of 3 years, which is quite reasonable given the long-term physics program planned at the ESS. The distance between the source and the detectors is taken to be 20 m. We make the conservative assumption of a detector signal acceptance of 80% above the nuclear recoil energy threshold.

The main properties of the different detectors considered in our analysis have been compiled in Ref. [43]; for convenience, we reproduce this information in Table I. In Table II, we quote the physical properties and the neutron rms radii of the target nuclei [57]. For recoil energy-sensitive detectors (CsI, Xe, Ge and Si), we use a Gaussian energy smearing for event reconstruction with a width $\sigma(T) = \sigma_0 \sqrt{T/T_{th}}$, where $\sigma_0 = (\Delta E/E)T_{th}$ is the energy resolution at the threshold (see Table I). Furthermore, following Ref. [43], we divide the range of reconstructed nuclear recoil energies into bins, taking the width of each bin to be twice the energy resolution at its center⁴, and compute the number of events bin by bin, applying the energy smearing between the true

⁴ For instance, for the CsI detector, the energy resolution at the center of the bin close to the peak of the event spectrum shown in Fig. 1 is $\sigma(T_{peak}) = \sigma_0 \sqrt{T_{peak}/T_{th}} \simeq 0.62 \text{ keV}$ (with $\sigma_0 = 0.3 \text{ keV}$ and $T_{th} = 1 \text{ keV}_{\text{nr}}$ from Table I, and $T_{peak} = 4.25 \text{ keV}_{\text{nr}}$), corresponding to a bin width of $1.24 \text{ keV}_{\text{nr}}$.

Detector technology	Target nucleus	Detector mass (kg)	Steady-state background	E_{th}^{ee} (keV _{ee})	QF (%)	T_{th} (keV _{nr})	$\frac{\Delta E}{E}$ (%) at T_{th}	σ_0 (keV)
Cryogenic scintillator	CsI	22.5	10 ckkd	0.1	10	1	30	0.3
High-pressure gaseous TPC	Xe	20	10 ckkd	0.18	20	0.9	40	0.36
Charge-coupled device	Si	1	1 ckkd	0.007	20	0.16	60	0.096
p-type point contact HPGe	Ge	7	15 ckkd	0.12	20	0.6	15	0.09
Scintillating bubble chamber	Ar	10	0.1 c/kg-day	–	–	0.1	40	0.04
Standard bubble chamber	C ₃ F ₈	10	15 c/kg-day	–	–	0.2	40	0.08

TABLE I. Main properties of the detectors proposed for CE ν NS measurements at the ESS: technology, target nucleus, detector mass, steady-state background, electron recoil energy threshold (E_{th}^{ee}), quenching factor (QF), nuclear recoil energy threshold (T_{th}), energy resolution at T_{th} in percent ($\Delta E/E$) and in keV (σ_0). Backgrounds (which do not include the 4×10^{-2} reduction by the ESS duty factor) are given in counts per kg and day for bubble chambers, for which only the total event rates are considered, while they are given in counts per keV, kg and day (ckkd) for the other detectors (keV_{ee} for the semiconductors Si and Ge, and keV_{nr} for CsI and Xe). All the information shown in this table is taken from Ref. [43]. More details about the detector characteristics, including the quenching factors, can be found in the same reference and in references therein.

Target nucleus	Z	N	Z/N	M (a.m.u)	R (fm)
Cs	55	78	0.71	132.91	4.83
I	53	74	0.72	126.90	4.83
Xe	54	78	0.69	131.29	4.79
Si	14	14	1	27.98	3.12
Ge	32	40	0.8	72.00	4.06
Ar	18	22	0.81	39.95	3.43
C	6	6	1	12.01	2.47
F	9	10	0.9	19.00	2.90

TABLE II. List of the target nuclei used in the detectors of Table I with their main properties: number of protons (Z) and neutrons (N), number of protons to neutrons ratio (Z/N), mass in atomic units (M) and neutron rms radius in fm (R).

and reconstructed recoil energies and the detection signal acceptance mentioned above. For bubble chamber detectors (Ar and C₃F₈), which lack energy resolution, we compute the total number of events above nuclear recoil energy threshold (assuming a signal acceptance of 80% as for the recoil energy-sensitive detectors); no binning or energy smearing is needed in that case.

B. Simulation procedure

In order to assess the statistical sensitivity to NSI parameters of the different detector setups at the ESS facility, we use the following χ^2 function:

$$\chi^2(\kappa) = \min_{\xi} \left[\sum_i 2 \left\{ N_i(\kappa, \xi) - \tilde{N}_i + \tilde{N}_i \ln \left(\frac{\tilde{N}_i}{N_i(\kappa, \xi)} \right) \right\} + \left(\frac{\xi_{sig}}{\sigma_{sig}} \right)^2 + \left(\frac{\xi_{bg}}{\sigma_{bg}} \right)^2 \right], \quad (11)$$

where i labels the different energy bins, \tilde{N}_i is the number of events in the i th bin predicted in the SM, and $N_i(\kappa, \xi)$ is the corresponding quantity in the presence of NSI parameters (collectively denoted by κ), including normalization factors, ξ_{sig} and ξ_{bg} , for the signal and background. Explicitly,

$$\tilde{N}_i = N_i^{sig}(SM) + N_i^{bg}, \quad N_i(\kappa, \xi) = N_i^{sig}(\kappa)(1 + \xi_{sig}) + N_i^{bg}(1 + \xi_{bg}), \quad (12)$$

where $N_i^{sig}(SM)$ and $N_i^{sig}(\kappa)$ are the numbers of signal events in the i th bin predicted by the SM and by the SM extension including NSIs, respectively, and N_i^{bg} is the number of background events in the same bin. The normalization factors, ξ_{sig} and ξ_{bg} , quantify the systematic errors, with associated uncertainties σ_{sig} and σ_{bg} . They are assumed to be the same for each bin, but independent of each other. Following Ref. [43], we assume σ_{sig} and σ_{bg} to be 10% and 1%, respectively.

The main source of background events is assumed to be the steady-state background, which is dominated by cosmic ray interactions. Beam-related backgrounds induced by the spallation neutrons and backgrounds from neutrino-induced neutrons have been neglected due to their small contributions. The expected level of steady-state backgrounds reported in Ref. [43] is indicated in Table I for each detection technology. For the CsI and Xe detectors, backgrounds are given in number of counts per keV_{nr}, per kg per day, while for the two semiconductors, Si and Ge, they are reported in number of counts per keV_{ee} per kg per day. In the latter case, we use the quenching factors given in Table I to convert the background value from keV_{ee} to keV_{nr}. For bubble chamber detectors, the backgrounds have been integrated above the nucleation threshold and are given in number of counts per kg and day.

IV. NUMERICAL RESULTS

In this section, we present our results for the expected sensitivities of the detectors listed in Table I to the NSI parameters $\varepsilon_{\alpha\beta}^{uV}$ and $\varepsilon_{\alpha\beta}^{dV}$ ($\alpha, \beta = e, \mu, \tau$) after 3 years of data taking at the ESS. Using Eq. (10), we first compute the CE ν NS signal rates predicted by the SM, as well as the expected background. Then we give the expected sensitivities of the different detectors to the NSI parameters taken one at a time, and quantify the improvement expected if two detectors operate simultaneously. Next we switch on a second NSI parameter, and show the future expected sensitivity of each detector in the corresponding two-dimensional parameter space. Finally, we show how using two detectors helps to partially break the degeneracies between different NSI parameters, and identify some of the most efficient detector combinations.

A. Event Spectra

In Fig. 1, we show the SM prediction for the CE ν NS signal rate as a function of the reconstructed nuclear recoil energy for the CsI, Si, Ge and Xe detectors described in Table I, assuming 3 years of data taking. The light, medium and dark blue histograms correspond to the contributions to the signal from the ν_μ , ν_e and $\bar{\nu}_\mu$ components of the ESS neutrino flux, respectively. The black curve represents the expected steady-state background as given in Table I; for presentation purposes,

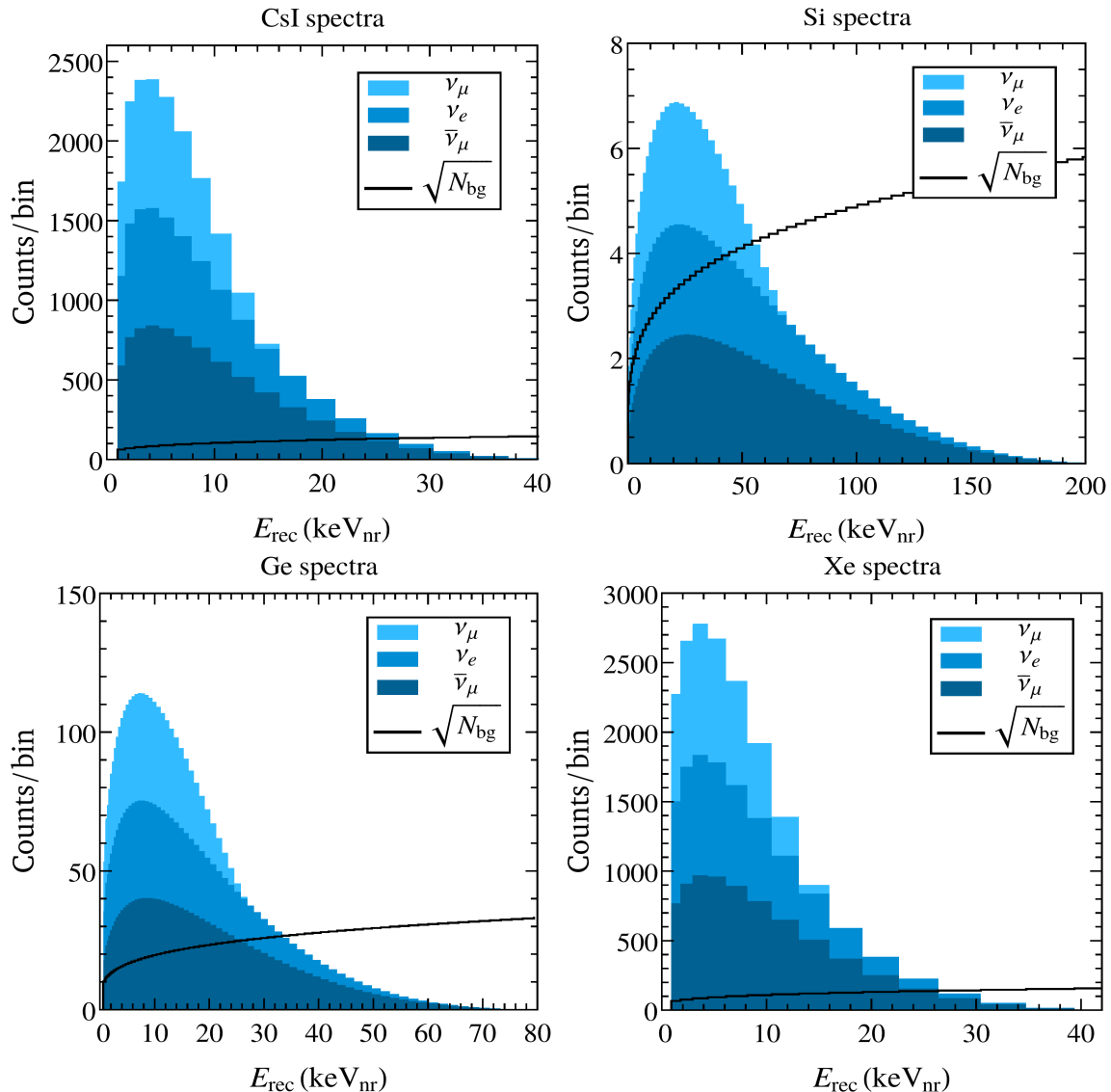


FIG. 1. Expected signal and background event spectra as a function of the reconstructed nuclear recoil energy for the CsI, Si, Ge and Xe detectors described in Table I, assuming 3 years of data taking. The signal events binning width is twice the energy resolution at its center, as explained in Section III A, and the contributions from the different components of the ESS neutrino flux are distinguished by the various shades of the colored regions. The expected steady-state background is represented by the black curve, which for presentation purposes shows the square root of the actual number of events.

the square root of the actual number of background events is shown. Notice that the CsI event spectrum shown in Fig. 1 perfectly agrees with the one displayed in Fig. 13 of Ref. [43].

Due to the long proton pulses of the ESS, it is impossible to distinguish experimentally between the contributions of the prompt and delayed components of the neutrino flux by using the additional timing information. However, above the maximal nuclear recoil energy that a prompt ν_μ can induce, only the delayed ν_e and $\bar{\nu}_\mu$ contribute to the signal events. As an example, for the Si detector, the ν_μ contribution sharply falls at the cut-off recoil energy $T_{prompt}^{max} = 2E_{prompt}^2/M_{Si} \simeq 68$ keV, where

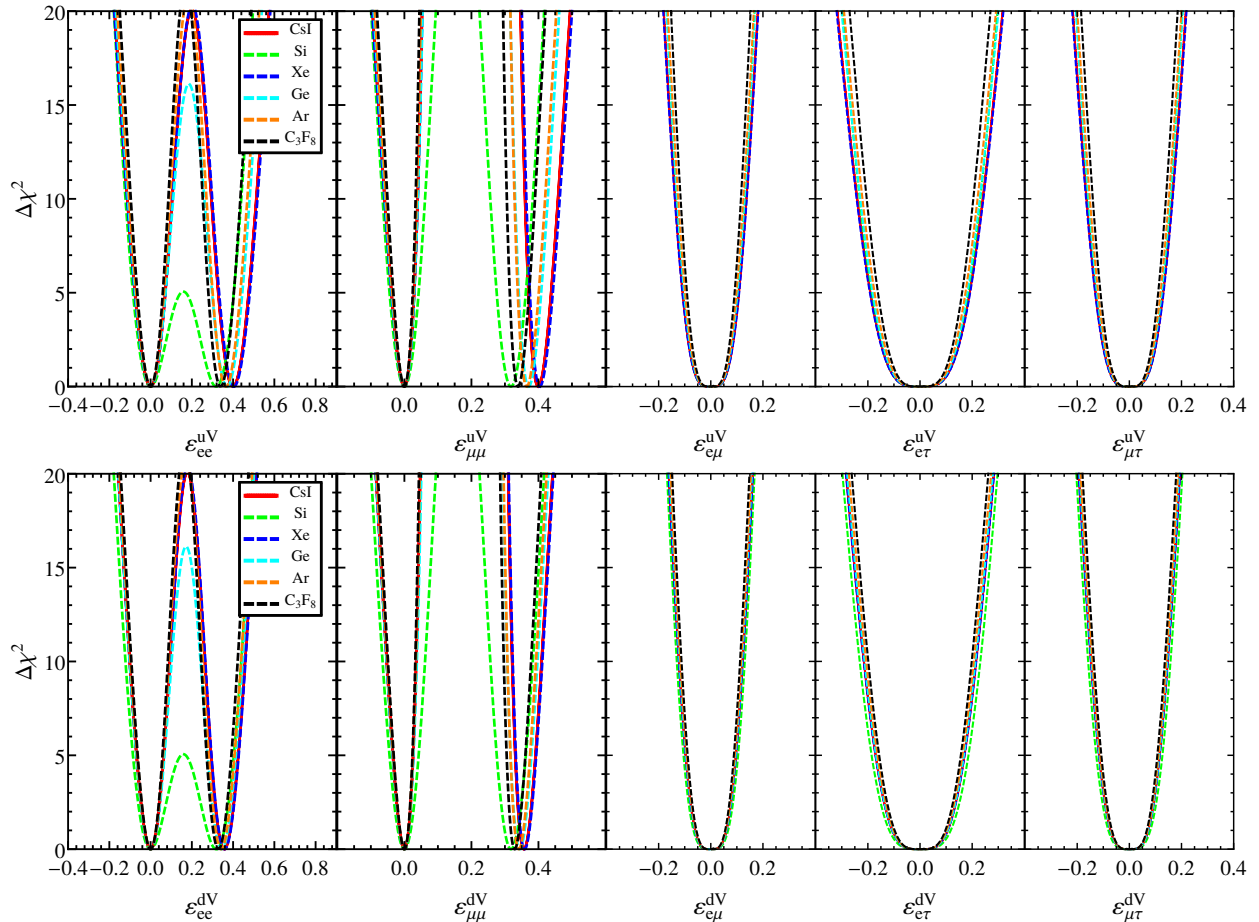


FIG. 2. One-dimensional projections of the expected sensitivities to the NSI parameters ε_{ee}^{qV} , $\varepsilon_{\mu\mu}^{qV}$, $\varepsilon_{e\mu}^{qV}$, $\varepsilon_{e\tau}^{qV}$ and $\varepsilon_{\mu\tau}^{qV}$ (with $q = u$ for the upper panel and $q = d$ for the lower panel) of the detectors described in Table I, assuming 3 years of data taking at the ESS. The red, green, blue, cyan, orange and black curves correspond to the CsI, Si, Xe, Ge, Ar and C_3F_8 targets, respectively. All off-diagonal NSI parameters are assumed to be real.

$E_{prompt} = (m_{\pi^+}^2 - m_{\mu}^2)/(2m_{\pi^+}) \simeq 29.8$ MeV is the energy of the monochromatic prompt neutrinos. A very small amount of ν_{μ} events can still be observed just above T_{prompt}^{max} due to the smearing by the energy resolution.

B. Detector sensitivities to NSI parameters

We are now ready to discuss the expected sensitivities to NSI parameters of the detectors described in Table I. By definition, CE ν NS can only probe NC-NSIs involving quarks, parametrized by the coefficients $\varepsilon_{\alpha\beta}^{uV}$ and $\varepsilon_{\alpha\beta}^{dV}$ ($\alpha, \beta = e, \mu, \tau$). Furthermore, since the ESS neutrino beam contains electron and muon (anti)neutrinos, but no tau neutrinos, only four out of six flavor-diagonal parameters can be constrained (namely, ε_{ee}^{qV} and $\varepsilon_{\mu\mu}^{qV}$, with $q = u$ or d). On the other hand, all six flavor off-diagonal parameters $\varepsilon_{e\mu}^{qV}$, $\varepsilon_{e\tau}^{qV}$ and $\varepsilon_{\mu\tau}^{qV}$ ($q = u, d$) contribute to the CE ν NS signal events. Throughout this work, we assume the off-diagonal NSI parameters to be real (the flavor diagonal

Target nucleus	Quark type	ε_{ee}^{qV}		$\varepsilon_{\mu\mu}^{qV}$	
		90% C.L.	2σ C.L.	90% C.L.	2σ C.L.
CsI	u	$[-0.055, 0.051]$ $\cup [0.35, 0.45]$	$[-0.067, 0.064]$ $\cup [0.34, 0.47]$	$[-0.027, 0.023]$ $\cup [0.38, 0.43]$	$[-0.034, 0.028]$ $\cup [0.37, 0.43]$
	d	$[-0.040, 0.047]$ $\cup [0.31, 0.41]$	$[-0.061, 0.057]$ $\cup [0.30, 0.42]$	$[-0.024, 0.020]$ $\cup [0.34, 0.38]$	$[-0.031, 0.024]$ $\cup [0.33, 0.39]$
Si	u	$[-0.063, 0.080]$ $\cup [0.24, 0.38]$	$[-0.077, 0.109]$ $\cup [0.21, 0.39]$	$[-0.032, 0.031]$ $\cup [0.29, 0.35]$	$[-0.039, 0.037]$ $\cup [0.28, 0.36]$
	d	$[-0.064, 0.08]$ $\cup [0.24, 0.38]$	$[-0.077, 0.11]$ $\cup [0.21, 0.39]$	$[-0.032, 0.031]$ $\cup [0.29, 0.35]$	$[-0.039, 0.038]$ $\cup [0.28, 0.36]$
Xe	u	$[-0.055, 0.052]$ $\cup [0.35, 0.46]$	$[-0.068, 0.063]$ $\cup [0.34, 0.47]$	$[-0.027, 0.023]$ $\cup [0.38, 0.43]$	$[-0.033, 0.026]$ $\cup [0.38, 0.44]$
	d	$[-0.049, 0.047]$ $\cup [0.31, 0.41]$	$[-0.061, 0.057]$ $\cup [0.30, 0.42]$	$[-0.025, 0.020]$ $\cup [0.34, 0.38]$	$[-0.03, 0.023]$ $\cup [0.34, 0.39]$
Ge	u	$[-0.054, 0.054]$ $\cup [0.32, 0.42]$	$[-0.066, 0.064]$ $\cup [0.30, 0.44]$	$[-0.026, 0.022]$ $\cup [0.35, 0.40]$	$[-0.032, 0.026]$ $\cup [0.34, 0.40]$
	d	$[-0.05, 0.049]$ $\cup [0.30, 0.39]$	$[-0.061, 0.06]$ $\cup [0.28, 0.40]$	$[-0.025, 0.021]$ $\cup [0.32, 0.37]$	$[-0.029, 0.025]$ $\cup [0.32, 0.37]$
Ar	u	$[-0.05, 0.047]$ $\cup [0.32, 0.42]$	$[-0.062, 0.058]$ $\cup [0.31, 0.43]$	$[-0.025, 0.021]$ $\cup [0.34, 0.39]$	$[-0.031, 0.024]$ $\cup [0.34, 0.40]$
	d	$[-0.047, 0.044]$ $\cup [0.30, 0.39]$	$[-0.058, 0.054]$ $\cup [0.29, 0.40]$	$[-0.024, 0.019]$ $\cup [0.32, 0.36]$	$[-0.029, 0.023]$ $\cup [0.32, 0.37]$
C_3F_8	u	$[-0.046, 0.043]$ $\cup [0.30, 0.39]$	$[-0.057, 0.053]$ $\cup [0.29, 0.40]$	$[-0.023, 0.019]$ $\cup [0.32, 0.36]$	$[-0.029, 0.023]$ $\cup [0.32, 0.37]$
	d	$[-0.045, 0.042]$ $\cup [0.29, 0.37]$	$[-0.055, 0.052]$ $\cup [0.28, 0.39]$	$[-0.023, 0.018]$ $\cup [0.31, 0.35]$	$[-0.028, 0.023]$ $\cup [0.31, 0.36]$

TABLE III. Expected sensitivities of the detectors described in Table I to the diagonal NSI parameters ε_{ee}^{qV} and $\varepsilon_{\mu\mu}^{qV}$ ($q = u, d$), at the 90% and 2σ confidence levels with one d.o.f. (i.e. $\Delta\chi^2 \leq 2.71$ and $\Delta\chi^2 \leq 4$, respectively), corresponding to the one-dimensional projections shown in Fig. 2. Experimental running time: 3 years.

ones are always real due to the hermiticity of the Lagrangian). In our analysis, we assume the true hypothesis to be the Standard Model, and we test nonzero NSI parameters against it. We therefore take $\Delta\chi^2 = \chi^2(\kappa)$, with $\chi^2(\kappa)$ the function defined in Eq. (11), and κ the set of NSI parameters assumed to be nonvanishing.

We start by considering a single NSI parameter at a time. In Fig. 2, we show the associated $\Delta\chi^2$ functions computed for each of the six detectors described in Table I. Each plot corresponds to a different nonvanishing NSI parameter (from left to right: ε_{ee}^{qV} , $\varepsilon_{\mu\mu}^{qV}$, $\varepsilon_{e\mu}^{qV}$, $\varepsilon_{e\tau}^{qV}$ and $\varepsilon_{\mu\tau}^{qV}$, with $q = u$ for the upper panel and $q = d$ for the lower panel). The red, green, blue, cyan, orange and black curves refer to the detectors with CsI, Si, Xe, Ge, Ar and C_3F_8 targets, respectively. One can see that, individually, all these targets have similar sensitivities, except for Si, whose sensitivity to the diagonal NSI parameters is slightly degraded due to low statistics. However, due to its proton to neutron ratio, which significantly differs from the ones of the other target nuclei

Target nucleus	Quark type	$\varepsilon_{e\mu}^{qV}$		$\varepsilon_{e\tau}^{qV}$		$\varepsilon_{\mu\tau}^{qV}$	
		90% C.L.	2σ C.L.	90% C.L.	2σ C.L.	90% C.L.	2σ C.L.
CsI	u	[-0.089, 0.089]	[-0.1, 0.1]	[-0.16, 0.16]	[-0.18, 0.18]	[-0.11, 0.11]	[-0.12, 0.12]
	d	[-0.08, 0.08]	[-0.09, 0.09]	[-0.14, 0.14]	[-0.16, 0.16]	[-0.096, 0.096]	[-0.11, 0.11]
Si	u	[-0.088, 0.088]	[-0.099, 0.099]	[-0.15, 0.15]	[-0.17, 0.17]	[-0.11, 0.11]	[-0.12, 0.12]
	d	[-0.088, 0.088]	[-0.098, 0.098]	[-0.15, 0.15]	[-0.17, 0.17]	[-0.11, 0.11]	[-0.12, 0.12]
Xe	u	[-0.09, 0.09]	[-0.1, 0.1]	[-0.16, 0.16]	[-0.18, 0.18]	[-0.11, 0.11]	[-0.12, 0.12]
	d	[-0.08, 0.08]	[-0.09, 0.09]	[-0.14, 0.14]	[-0.16, 0.16]	[-0.097, 0.097]	[-0.11, 0.11]
Ge	u	[-0.085, 0.085]	[-0.096, 0.096]	[-0.15, 0.15]	[-0.17, 0.17]	[-0.1, 0.1]	[-0.11, 0.11]
	d	[-0.079, 0.079]	[-0.088, 0.088]	[-0.14, 0.14]	[-0.16, 0.16]	[-0.095, 0.095]	[-0.11, 0.11]
Ar	u	[-0.082, 0.082]	[-0.092, 0.092]	[-0.14, 0.14]	[-0.16, 0.16]	[-0.099, 0.099]	[-0.11, 0.11]
	d	[-0.077, 0.077]	[-0.086, 0.086]	[-0.13, 0.13]	[-0.15, 0.15]	[-0.093, 0.093]	[-0.1, 0.1]
C ₃ F ₈	u	[-0.075, 0.075]	[-0.085, 0.085]	[-0.13, 0.13]	[-0.15, 0.15]	[-0.092, 0.092]	[-0.1, 0.1]
	d	[-0.073, 0.073]	[-0.083, 0.083]	[-0.13, 0.13]	[-0.15, 0.15]	[-0.089, 0.089]	[-0.1, 0.1]

TABLE IV. Expected sensitivities of the detectors described in Table I to the off-diagonal NSI parameters $\varepsilon_{e\mu}^{qV}$, $\varepsilon_{e\tau}^{qV}$ and $\varepsilon_{\mu\tau}^{qV}$ ($q = u, d$), at the 90% and 2σ confidence levels with one d.o.f. (i.e. $\Delta\chi^2 \leq 2.71$ and $\Delta\chi^2 \leq 4$, respectively), corresponding to the one-dimensional projections shown in Fig. 2. Experimental running time: 3 years. All NSI parameters are assumed to be real.

considered, the Si nucleus will have a significant impact when combining the results of different detectors, as we will see later. In Table III, we give the expected sensitivity of each detector to the diagonal NSI parameters at the 90% and 2σ confidence levels with one degree of freedom (d.o.f.), i.e. $\Delta\chi^2 \leq 2.71$ and $\Delta\chi^2 \leq 4$, respectively. For each parameter, two disconnected regions of values appear, associated with the two minima of the $\Delta\chi^2$. Finally, Table IV shows the expected sensitivities to the off-diagonal NSI parameters. In this case, there is a single region of expected allowed values for each parameter, centered around zero. These expected sensitivities represent a substantial improvement with respect to the constraints extracted from the current COHERENT results [9, 17].

Let us now see how combining two detectors with different target materials can improve the sensitivity to NSI parameters. In Fig. 3, we show the $\Delta\chi^2$ functions computed by combining the event spectra of two detectors. As in Fig. 2, each plot corresponds to a different nonvanishing NSI

Target nucleus	Quark type	ε_{ee}^{qV}		$\varepsilon_{\mu\mu}^{qV}$	
		90% C.L.	2 σ C.L.	90% C.L.	2 σ C.L.
CsI + Si	u	[-0.041, 0.042] –	[-0.05, 0.052] \cup [0.34, 0.39]	[-0.02, 0.016] –	[-0.025, 0.022] –
	d	[-0.038, 0.039] \cup [0.31, 0.38]	[-0.046, 0.047] \cup [0.30, 0.39]	[-0.018, 0.015] –	[-0.023, 0.02] \cup [0.34, 0.36]

TABLE V. Same as Table III, but for the combined analysis of the CsI and Si detectors, shown in Fig. 3.

Target nucleus	Quark type	$\varepsilon_{e\mu}^{qV}$		$\varepsilon_{e\tau}^{qV}$		$\varepsilon_{\mu\tau}^{qV}$	
		90% C.L.	2 σ C.L.	90% C.L.	2 σ C.L.	90% C.L.	2 σ C.L.
CsI+Si	u	[-0.074, 0.074]	[-0.081, 0.081]	[-0.13, 0.13]	[-0.14, 0.14]	[-0.09, 0.09]	[-0.10, 0.10]
	d	[-0.068, 0.068]	[-0.075, 0.075]	[-0.12, 0.12]	[-0.14, 0.14]	[-0.085, 0.085]	[-0.092, 0.092]

TABLE VI. Same as Table IV, but for the combined analysis of the CsI and Si detectors, shown in Fig. 3.

parameter (from left to right: ε_{ee}^{qV} , $\varepsilon_{\mu\mu}^{qV}$, $\varepsilon_{e\mu}^{qV}$, $\varepsilon_{e\tau}^{qV}$ and $\varepsilon_{\mu\tau}^{qV}$, with $q = u$ for the upper panel and $q = d$ for the lower panel). For simplicity, we consider only a few out of the many possible combinations between the six detectors, which we choose among the most efficient ones in terms of sensitivity improvement. The red, green, blue, cyan and magenta curves refer to the combinations CsI + Xe, CsI + Si, Xe + Si, Ge + Si and CsI + C₃F₈, respectively. As can be seen from these plots, the most significant sensitivity improvement with respect to the setup with a single detector is obtained from the combination CsI + Si, especially for the parameters ε_{ee}^{uV} , $\varepsilon_{\mu\mu}^{uV}$ and $\varepsilon_{\mu\mu}^{dV}$. In Tables V and VI, we give the expected sensitivities of this particular combination of detectors to the diagonal and off-diagonal NSI parameters, respectively. As can be seen by comparing these expected sensitivities with the ones appearing in Tables III and IV, the improvement is significant for the off-diagonal parameters, and even more remarkable for some of the diagonal parameters. For instance, the expected allowed region around 0.3 – 0.4 for $\varepsilon_{\mu\mu}^{uV}$ in Table III can be excluded at more than 3 σ by the combination CsI + Si. By contrast, the analogous regions for ε_{ee}^{uV} and $\varepsilon_{\mu\mu}^{dV}$ can only be excluded at the 90% confidence level.

NC-NSI parameters are also constrained by neutrino oscillation experiments, as they modify neutrino propagation in matter [56, 58]. However, while CE ν NS is only sensitive to the parameters $\epsilon_{\alpha\beta}^{uV}$ and $\epsilon_{\alpha\beta}^{dV}$, oscillation data also depend on the neutrino couplings to electrons, $\epsilon_{\alpha\beta}^{eV}$. More precisely, the Hamiltonian in matter depends on the combinations of NSI parameters $\epsilon_{\alpha\beta}^m(x) \equiv \epsilon_{\alpha\beta}^{eV} + \epsilon_{\alpha\beta}^{pV} + Y_n(x) \epsilon_{\alpha\beta}^{nV}$, where $\epsilon_{\alpha\beta}^{pV} = 2\epsilon_{\alpha\beta}^{uV} + \epsilon_{\alpha\beta}^{dV}$, $\epsilon_{\alpha\beta}^{nV} = \epsilon_{\alpha\beta}^{uV} + 2\epsilon_{\alpha\beta}^{dV}$, and the x -dependence comes from the varying chemical composition of the medium, $Y_n(x) = n_n(x)/n_p(x)$ (with $n_n(x)$ and $n_p(x)$ the neutron and proton densities). Furthermore, only the differences of diagonal NSI parameters are constrained by oscillation data. In addition to giving a more direct access to non-standard neutrino couplings to quarks, CE ν NS measurements are crucial to discriminate between the LMA and the LMA-Dark explanations of neutrino oscillation data [59, 60]. In Refs. [61–63], a combined analysis of oscillation data and of the COHERENT results was performed under the assumption that all $\epsilon_{\alpha\beta}^e$ parameters

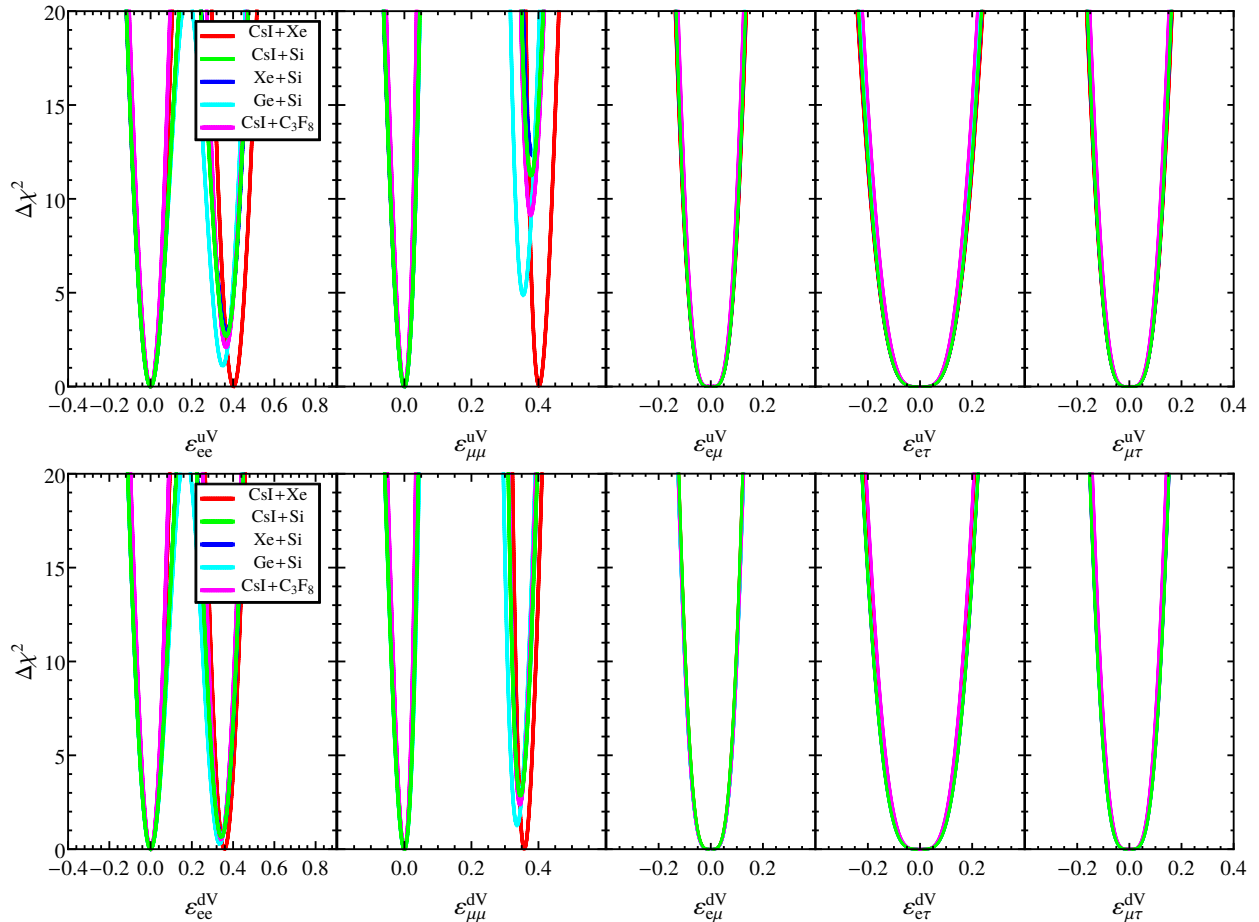


FIG. 3. One-dimensional projections of the expected sensitivities to the NSI parameters ϵ_{ee}^{qV} , $\epsilon_{\mu\mu}^{qV}$, $\epsilon_{e\mu}^{qV}$, $\epsilon_{e\tau}^{qV}$ and $\epsilon_{\mu\tau}^{qV}$ (with $q = u$ for the upper panel and $q = d$ for the lower panel) of the detectors described in Table I, assuming 3 years of data taking at the ESS. The red, green, blue, cyan and magenta curves correspond to the CsI + Xe, CsI + Si, Xe + Si, Ge + Si and CsI + C₃F₈ target combinations, respectively. All off-diagonal NSI parameters are assumed to be real.

vanish and that the non-standard neutrino couplings to up and down quarks are proportional to each other, $\epsilon_{\alpha\beta}^{uV} \propto \epsilon_{\alpha\beta}^{dV}$. It should be kept in mind that the associated bounds on NSI parameters do depend on these assumptions and cannot be directly compared with the expected sensitivities from future CE ν NS experiments at the ESS discussed in this paper.

C. Breaking degeneracies in the presence of two NSI parameters

We now move on to study the case where two NSI parameters are different from zero at a time. As can be expected, the sensitivity of a single detector is strongly limited by the existence of degeneracies between the two parameters. These degeneracies are a consequence of the fact that (considering for simplicity a single-nucleus target) the number of CE ν NS events in each energy bin depends only on two nucleus-dependent combinations of NSI parameters, $(Q_{W,e}^V)^2$ and $(Q_{W,\mu}^V)^2$, defined in Eq. (9). As a result, it is not possible to experimentally distinguish between different

sets of NSI parameter values giving the same $(Q_{W,e}^V)^2$ and $(Q_{W,\mu}^V)^2$; this is called a degeneracy, and it results in extended allowed regions in two-parameter sensitivity plots obtained from a single nuclear target⁵. We will however see that combining the event spectra of two suitably chosen detectors can significantly improve the experimental sensitivity and partially break these degeneracies.

Let us first consider the individual detector sensitivities. In Fig. 4, we choose the two independent NSI parameters to be ε_{ee}^{qV} and $\varepsilon_{\mu\mu}^{q'V}$, with $q, q' \in \{u, d\}$, and we show the expected regions allowed by the different detectors at 90% C.L. in the corresponding parameter space. Each row is associated with a different combination: from top to bottom, $(\varepsilon_{ee}^{uV}, \varepsilon_{\mu\mu}^{uV})$, $(\varepsilon_{ee}^{dV}, \varepsilon_{\mu\mu}^{dV})$, $(\varepsilon_{ee}^{uV}, \varepsilon_{\mu\mu}^{dV})$ and $(\varepsilon_{ee}^{dV}, \varepsilon_{\mu\mu}^{uV})$. The green, red and blue regions in the left panels correspond to the CsI, Ar and C_3F_8 detectors, while the cyan, magenta, and orange regions in the right panels correspond to the Xe, Ge, and Si detectors, respectively. Notice that these colored regions share a characteristic elliptical (or approximately elliptical) shape. This is easily explained for single-target bubble chambers, like the Ar detector of Table I, for which the analysis uses only the total number of events. Assuming e.g. $\varepsilon_{ee}^{uV} \neq 0$ and $\varepsilon_{\mu\mu}^{uV} \neq 0$, the predicted total number of signal events can be expressed as

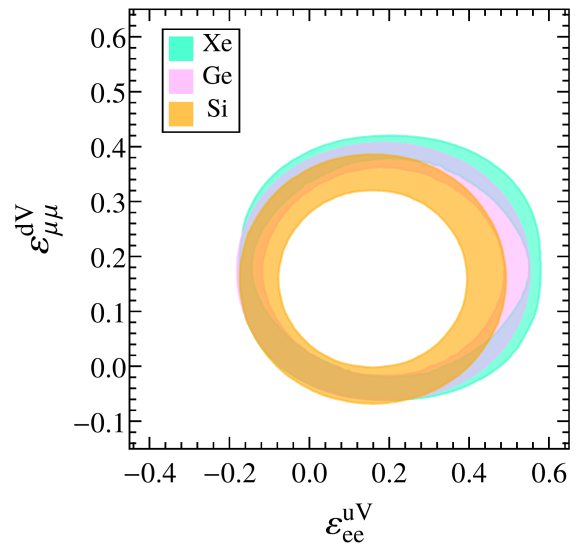
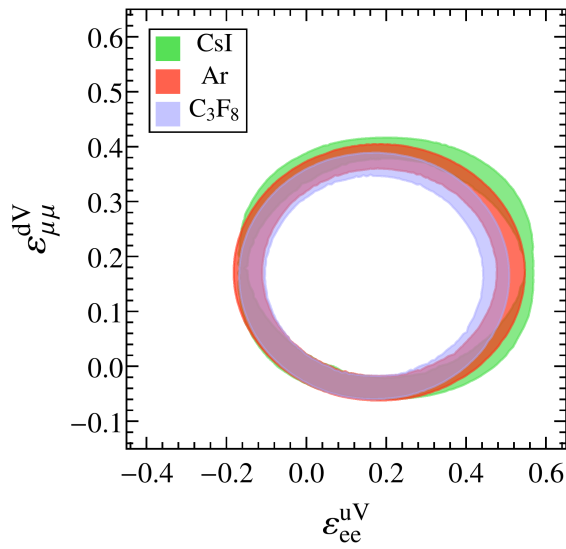
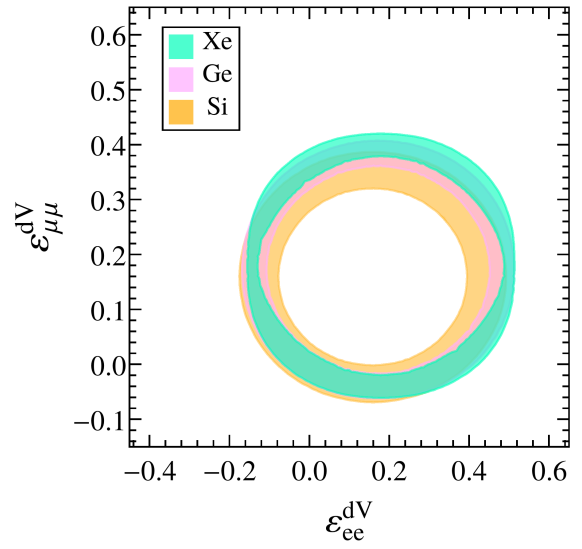
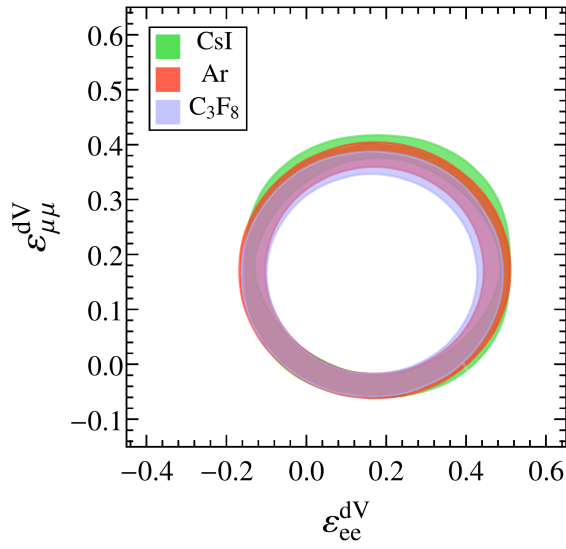
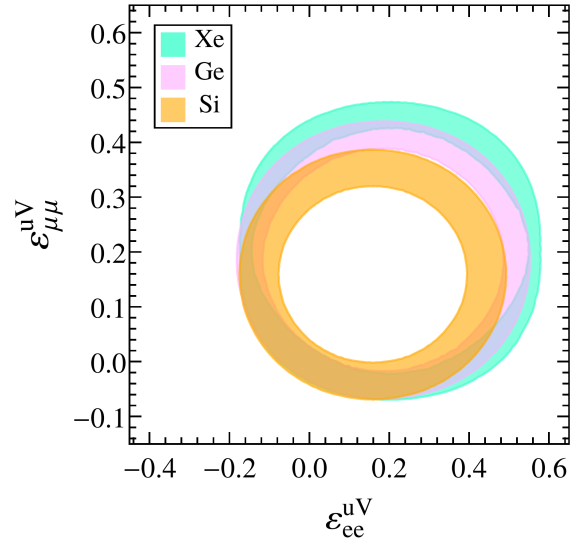
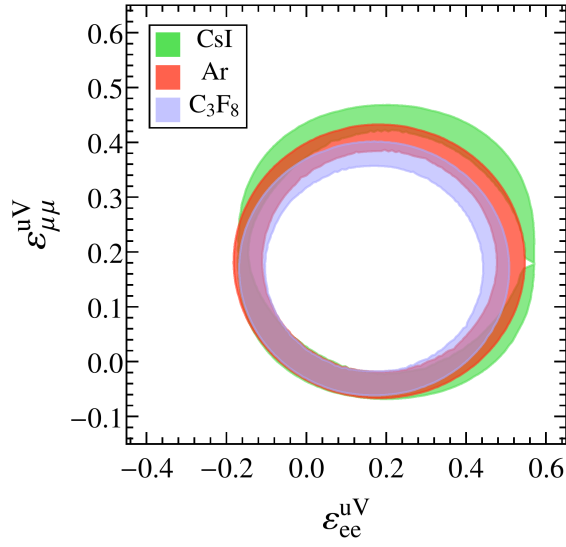
$$N_{th} = C_e (2Z + N)^2 \left(\varepsilon_{ee}^{uV} + \frac{Zg_V^p + Ng_V^n}{2Z + N} \right)^2 + C_\mu (2Z + N)^2 \left(\varepsilon_{\mu\mu}^{uV} + \frac{Zg_V^p + Ng_V^n}{2Z + N} \right)^2, \quad (13)$$

where C_e (C_μ) is the constant that results from performing the integral over E_{ν_e} (E_{ν_μ} and $E_{\bar{\nu}_\mu}$) in Eq. (10), after factorizing the weak nuclear charge (given by Eq. (9)) out of the $CE\nu$ NS cross-section. For a fixed number of events N_{th} , Eq. (13) is the equation of an ellipse with minor and major semi-axes given by $\sqrt{N_{th}/C_e (2Z + N)^2}$ and $\sqrt{N_{th}/C_\mu (2Z + N)^2}$, respectively. Values of ε_{ee}^{uV} and $\varepsilon_{\mu\mu}^{uV}$ lying on the same ellipse reproduce the same number of events N_{th} , hence the same value of χ^2 in Eq. (11): they are degenerate from the point of view of $CE\nu$ NS measurements. The expected 90% C.L. sensitivity region associated with the Ar detector in the first row of Fig. 4 is therefore the collection of all ellipses satisfying $\Delta\chi^2 \leq 4.61$. The same arguments apply to the other three combinations of the ε_{ee}^{qV} and $\varepsilon_{\mu\mu}^{q'V}$ parameters, and explain the elliptical shape of the Ar regions in Fig. 4.

The above discussion can be generalized to bubble chamber detectors with two nuclei, like C_3F_8 , where it is also possible to write the predicted number of events as the equation of an ellipse, with more complicated expressions for the axes. For recoil energy-sensitive detectors (CsI, Xe, Si and Ge), the analysis is done bin by bin, and the ellipses defined by Eq. (13) do not necessarily explain accurately the shape of the 90% C.L. sensitivity regions displayed in Fig. 4. Indeed, while two points on one of these ellipses correspond to the same total number of events, they may not predict the same recoil energy distribution, hence their χ^2 value may slightly differ. This explains, for instance, why the sensitivity regions for CsI and Xe are squeezed at some points.

In Fig. 5, we show the expected 90% C.L. sensitivities for the remaining two possible combinations of diagonal NSI parameters, namely $(\varepsilon_{\alpha\alpha}^{uV}, \varepsilon_{\alpha\alpha}^{dV})$ with $\alpha = e$ or μ . These regions are composed of two parallel linear bands [15], a fact that can be explained again from the expressions of the

⁵ In practice, degeneracies also arise between different sets of NSI parameter values giving the same total number of events, but different values for $(Q_{W,e}^V)^2$ and $(Q_{W,\mu}^V)^2$. This is a consequence of the experimental difficulty to distinguish between the contribution of ν_e (which depends on $(Q_{W,e}^V)^2$) from the one of ν_μ and $\bar{\nu}_\mu$ (which depends on $(Q_{W,\mu}^V)^2$). This is the case, for instance, of the degeneracies observed between the parameters ε_{ee}^{qV} and $\varepsilon_{\mu\mu}^{q'V}$ ($q, q' = u, d$) in Fig. 4.



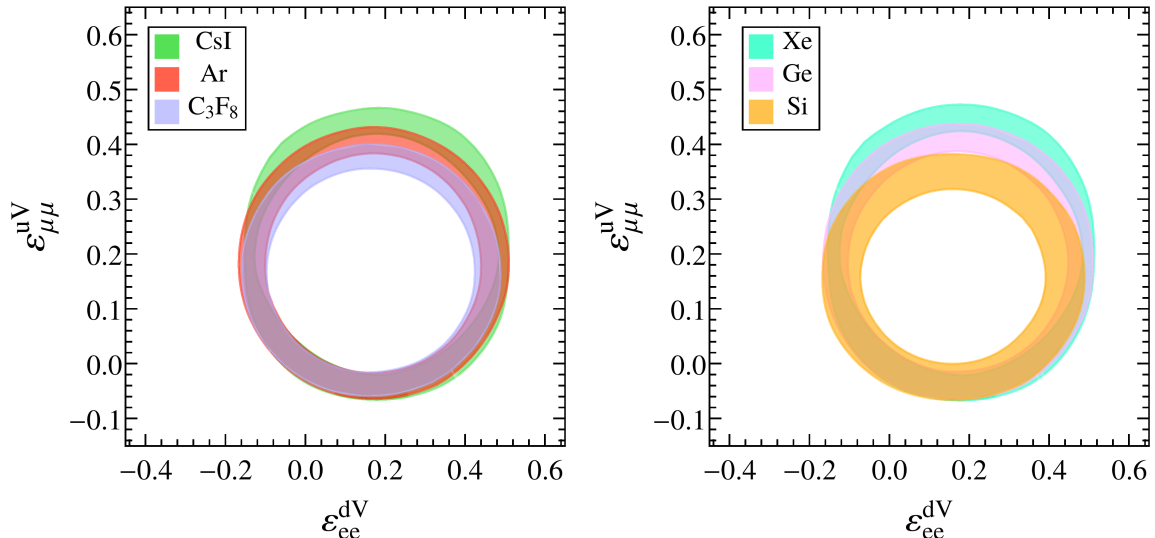


FIG. 4. Expected 90% C. L. sensitivities (with two d.o.f., i.e. $\Delta\chi^2 \leq 4.61$) to different combinations of two diagonal NSI parameters for the detectors described in Table I. We assume 3 years of data taking at the ESS. Each color is associated with a specific detector: CsI (green), Ar (red), Xe (cyan), Ge (magenta), Si (orange) and C_3F_8 (blue). The plots in the first, second, third and fourth rows correspond to the combinations $(\varepsilon_{ee}^{uV}, \varepsilon_{\mu\mu}^{uV})$, $(\varepsilon_{ee}^{dV}, \varepsilon_{\mu\mu}^{dV})$, $(\varepsilon_{ee}^{uV}, \varepsilon_{\mu\mu}^{dV})$ and $(\varepsilon_{ee}^{dV}, \varepsilon_{\mu\mu}^{uV})$, respectively.

weak nuclear charge and differential CE ν NS event rate in Eqs. (9) and (10), respectively. Indeed, assuming for instance the two nonvanishing NSI parameters to be ε_{ee}^{uV} and ε_{ee}^{dV} , we can write the predicted total number of signal events as (for a single-nucleus detector)

$$N_{th} = \left[Zg_V^p + Ng_V^n + (2Z + N)\varepsilon_{ee}^{uV} + (Z + 2N)\varepsilon_{ee}^{dV} \right]^2 C_e + \left[Zg_V^p + Ng_V^n \right]^2 C_\mu, \quad (14)$$

where C_e and C_μ are the same constants that appear in Eq. (13). For fixed N_{th} , Eq. (14) describes two straight lines in the $(\varepsilon_{ee}^{uV}, \varepsilon_{ee}^{dV})$ plane, with a common slope m given by [14]

$$m = -\frac{2Z + N}{Z + 2N} \quad (15)$$

(obviously, a similar conclusion holds if the two nonvanishing NSI parameters are chosen to be $\varepsilon_{\mu\mu}^{uV}$ and $\varepsilon_{\mu\mu}^{dV}$ rather than ε_{ee}^{uV} and ε_{ee}^{dV}). For recoil energy-sensitive detectors, there is an equation analogous to Eq. (14) for each bin i , with N_{th} , C_e and C_μ replaced by bin-dependent quantities N_{th}^i , C_e^i and C_μ^i , but the slope, still given by Eq. (15), is the same for all bins⁶. Thus, irrespective of the detection technique, each expected 90% C.L. allowed region in Fig. 5 is the collection of all line intervals with slope m satisfying $\Delta\chi^2 \leq 4.61$ (where both m and the function $\Delta\chi^2 = \chi^2(\varepsilon_{ee}^{uV}, \varepsilon_{ee}^{dV})$ depend on the detector). This explains why these regions are made of two parallel bands.

Finally, in Fig. 6, we show the expected 90% C.L. sensitivities for the combinations of off-diagonal NSI parameters $(\varepsilon_{\alpha\beta}^{uV}, \varepsilon_{\alpha\beta}^{dV})$, $\alpha \neq \beta$. In this case, the sensitivity regions are single linear

⁶ The situation is more subtle for detectors made of two nuclei, but in practice the slopes associated with each nucleus are very close, both for CsI and for C_3F_8 .

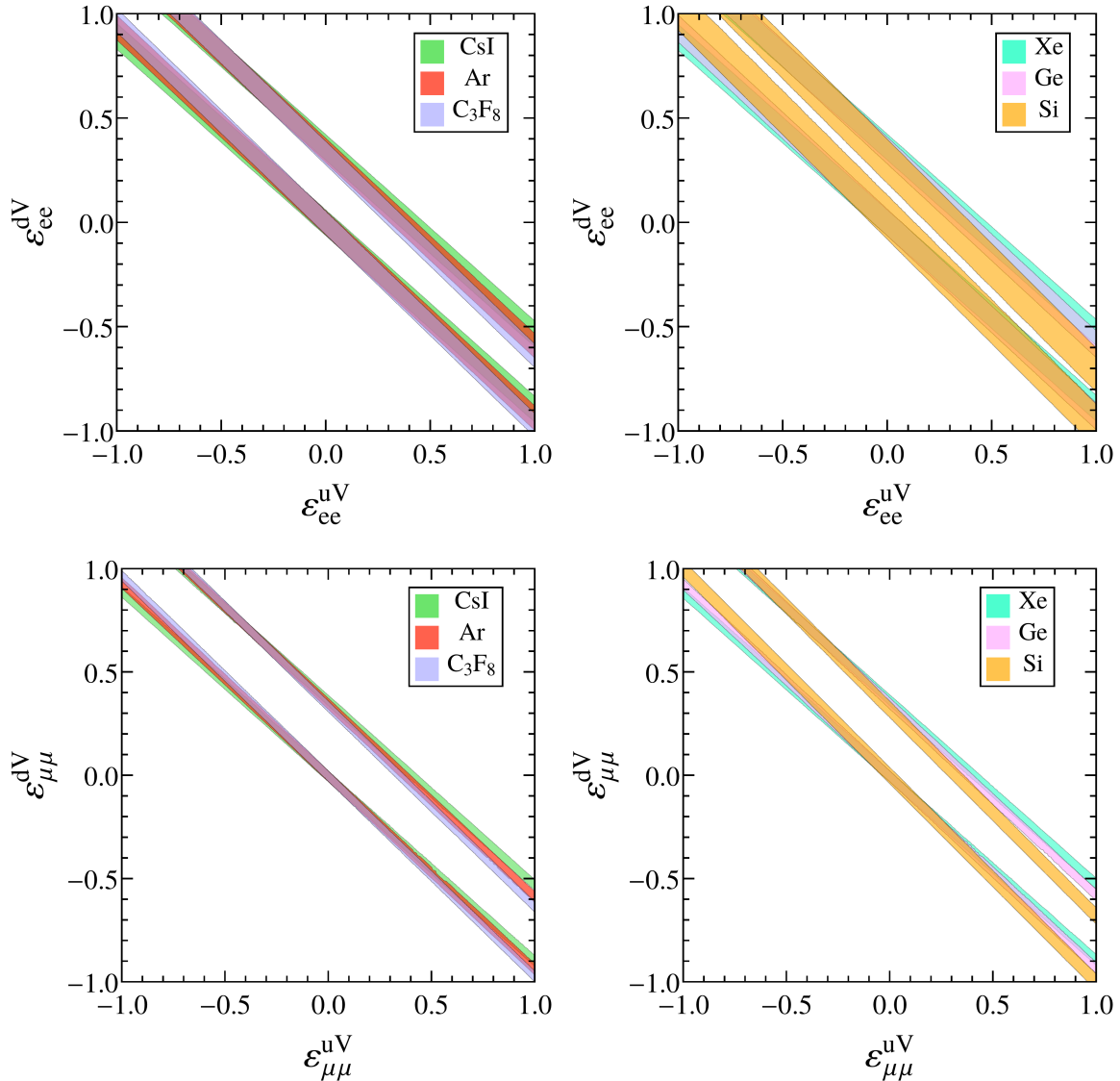


FIG. 5. Expected 90% C. L. sensitivities (with two d.o.f., i.e. $\Delta\chi^2 \leq 4.61$) to different combinations of two diagonal NSI parameters for the detectors described in Table I. We assume 3 years of data taking at the ESS. The color code is the same as in Fig. 4. The top panels correspond to the combinations $(\varepsilon_{ee}^{uV}, \varepsilon_{ee}^{dV})$, and the bottom panels to $(\varepsilon_{\mu\mu}^{uV}, \varepsilon_{\mu\mu}^{dV})$.

bands, which can be understood from arguments similar to the ones used above. Indeed, assuming the two nonvanishing NSI parameters to be $\varepsilon_{e\mu}^{uV}$ and $\varepsilon_{e\mu}^{dV}$, one can write the expected total number of signal events in the form (for a single-nucleus detector)

$$N_{th} = C \left\{ [Zg_V^p + Ng_V^n]^2 + [(2Z + N)\varepsilon_{e\mu}^{uV} + (Z + 2N)\varepsilon_{e\mu}^{dV}]^2 \right\}, \quad (16)$$

where C is the constant that results from performing the integral over all three neutrino fluxes in Eq. (10) after factorizing out the weak nuclear charge. For a fixed number of events N_{th} , Eq. (16) describes two straight lines in the $(\varepsilon_{e\mu}^{uV}, \varepsilon_{e\mu}^{dV})$ plane, symmetric under a reflection through the origin

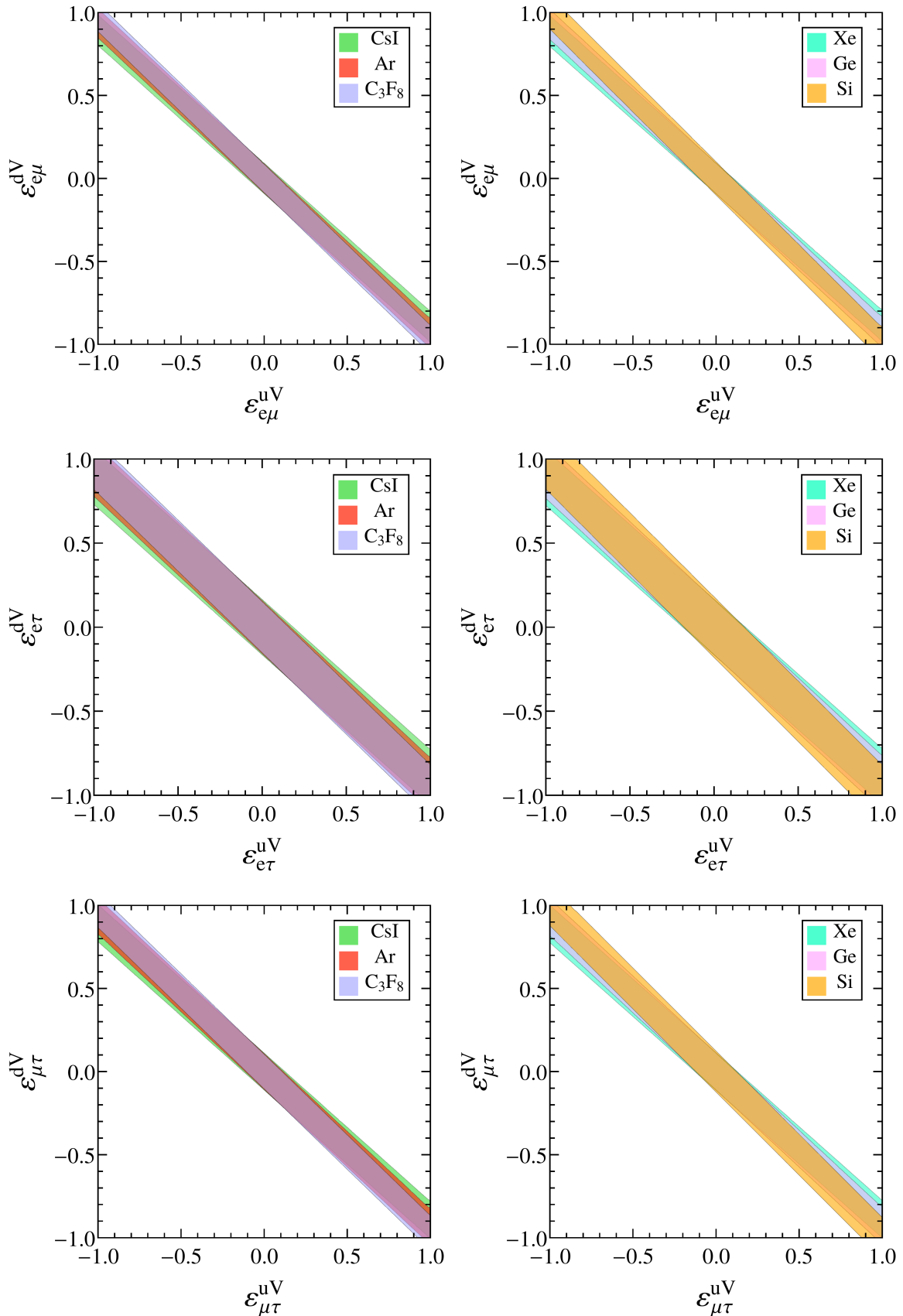


FIG. 6. Expected 90% C. L. sensitivities (with two d.o.f., i.e. $\Delta\chi^2 \leq 4.61$) to different combinations of two diagonal NSI parameters for the detectors described in Table I. We assume 3 years of data taking at the ESS. The color code is the same as in Fig. 4. The top, central and bottom panels correspond to the combinations $(\varepsilon_{e\mu}^{uV}, \varepsilon_{e\mu}^{dV})$, $(\varepsilon_{e\tau}^{uV}, \varepsilon_{e\tau}^{dV})$ and $(\varepsilon_{\mu\tau}^{uV}, \varepsilon_{\mu\tau}^{dV})$, respectively.

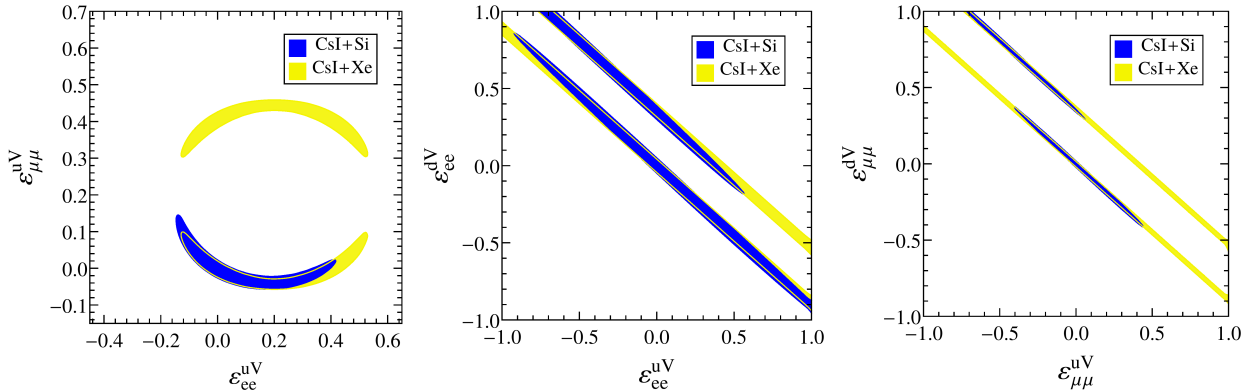


FIG. 7. Expected 90% C. L. sensitivities (with two d.o.f., i.e. $\Delta\chi^2 \leq 4.61$), in the planes defined by different sets of two diagonal NSI parameters, allowed by the combinations of detectors CsI + Xe (yellow) and CsI + Si (blue), assuming 3 years of data taking at the ESS for each detector. The left, central and right panels correspond to the parameters $(\varepsilon_{ee}^{uV}, \varepsilon_{\mu\mu}^{uV})$, $(\varepsilon_{ee}^{uV}, \varepsilon_{ee}^{dV})$ and $(\varepsilon_{\mu\mu}^{uV}, \varepsilon_{\mu\mu}^{dV})$, respectively.

and with a slope m again given by Eq. (15). For $N_{th} = N_{th}^{SM} = C(Zg_V^p + Ng_V^n)^2$, the two lines merge into a single one crossing the origin. Similar conclusions hold if the two nonvanishing NSI parameters are chosen to be $(\varepsilon_{e\tau}^{uV}, \varepsilon_{e\tau}^{dV})$ or $(\varepsilon_{\mu\tau}^{uV}, \varepsilon_{\mu\tau}^{dV})$. Omitting detailed explanations analogous to the ones given for Fig. 5, this explains why the expected 90% C.L. sensitivity regions in Fig. 6 consist of a single linear band of slope m containing the origin.

As can be seen from Figs. 4, 5 and 6, degeneracies between different NSI parameters appear whenever one tries to constrain more than one parameter at a time from a single CE ν NS measurement experiment. We now show how these degeneracies can be partially lifted when combining the results of two different detectors. Given the large number of possible combinations of two detectors, we restrict our study to a few suitably chosen cases. Already from inspecting how the different sensitivity regions in Figs. 4 to 6 overlap, one can identify some more favorable combinations. In particular, detectors with a different proton to neutron ratio [14] help to reduce the degeneracies in Figs. 5 and 6, as the associated bands are characterized by different slopes (indeed, m can be written as $m = -(2r + 1)(r + 2)$, where $r = Z/N$). As an illustration, we show in Fig. 7 the expected 90% C.L. sensitivities in the parameter spaces $(\varepsilon_{ee}^{uV}, \varepsilon_{\mu\mu}^{uV})$, $(\varepsilon_{ee}^{uV}, \varepsilon_{ee}^{dV})$ and $(\varepsilon_{\mu\mu}^{uV}, \varepsilon_{\mu\mu}^{dV})$ for the detector combinations CsI + Si, and CsI + Xe. As can be seen, the most efficient combination is the one involving two target materials with a very different proton to neutron ratio ($r = 0.71$ [0.72] for Cs [I] versus $r = 1$ for Si, while Xe has $r = 0.69$, very close to the Cs and I nuclei). Moreover, by comparing the blue area on the left plot of Fig. 7 with Fig. 14 of Ref. [43], one can see that combining the data of two detectors with different enough characteristics, such as CsI and Si, is much more efficient in breaking degeneracies than filling the same gas TPC detector alternatively with Xe and Ar, which is the option studied in Ref. [43]. To make the comparison more meaningful, we checked that this conclusion still holds if the CsI and Si detectors run only for 1.5 years each, as for the gas TPC detector filled with either Xe or Ar.

For comparison, we show in Fig. 8 a few more combinations of two detectors, again chosen among the most suitable ones to reduce degeneracies between two different NSI parameters. Among these

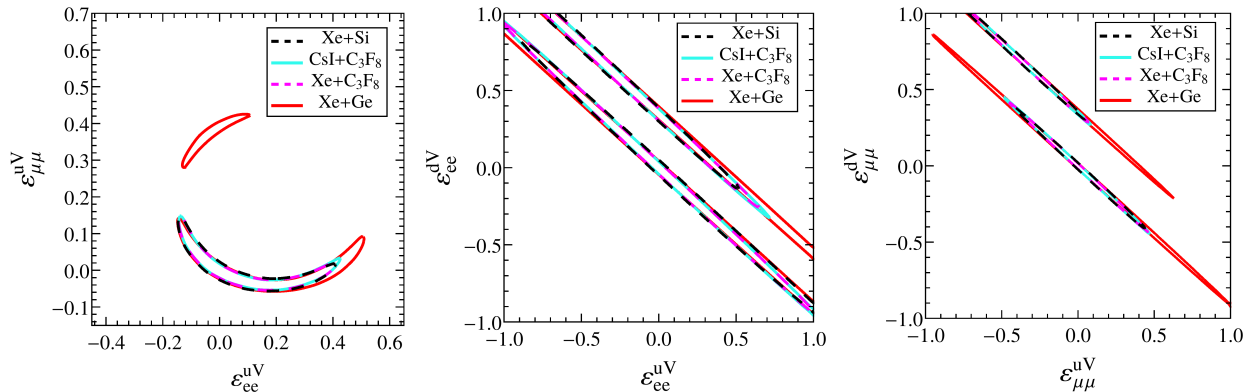


FIG. 8. Same as Fig. 7 for different combinations of two detectors: Xe + Si (dashed black), CsI + C₃F₈ (solid cyan), Xe + C₃F₈ (dashed magenta) and Xe + Ge (solid red).

combinations, Xe + Si is comparable to CsI + Si, while CsI + C₃F₈ and Xe + C₃F₈ are almost as efficient. On the other hand, Xe + Ge is significantly less sensitive, but still better than CsI + Xe. These results are expected from the previous discussion regarding the impact of the proton to neutron ratio of the targets: the combinations that have very different ratios are more suitable to break degeneracies between NSI parameters.

Finally, we briefly comment on degeneracies between off-diagonal NSI parameters. As can be seen from Fig. 6, the sensitivity regions for the pairs of NSI parameters $(\varepsilon_{\alpha\beta}^{uV}, \varepsilon_{\alpha\beta}^{dV})$, $\alpha \neq \beta$, are just a little bit tilted with respect to each other and overlap to a large extent⁷. Therefore, combining the data from two different detectors does not lead to a significant reduction of degeneracies between these parameters. An even stronger conclusion holds for pairs of off-diagonal NSI parameters with different flavour indices, such as $(\varepsilon_{e\mu}^{uV}, \varepsilon_{e\tau}^{uV})$, whose contributions to the CE ν NS cross section do not interfere: in this case, the only benefit of combining the data from two different detectors is the increase in statistics. However, when a diagonal and an off-diagonal NSI parameters are assumed to be simultaneously nonvanishing, combining two suitably chosen detectors does lead to a partial breaking of degeneracies, as can be seen from the plots in Fig. 9.

V. CONCLUSIONS

In this work, we explored the physics potential of the European Spallation Source setup in constraining non-standard neutrino interactions using coherent elastic neutrino-nucleus scattering. More specifically, we studied the sensitivity that different detectors can achieve on NC-NSI parameters after 3 years of data taking, using the ESS neutrino beam as a source for high-statistics CE ν NS measurements. These detectors, proposed in Ref. [43], use different detection technologies with various target materials (CsI, Xe, Si, Ge, Ar and C₃F₈) and are characterized by different recoil energy thresholds. We first showed that these detectors could ameliorate the bounds on

⁷ This large overlap is due to the fact that the contribution of off-diagonal NSI parameters to the CE ν NS cross section arises at order ε^2 , as can be seen from Eq. (16). By contrast, the contribution of diagonal NSI parameters is of order ε due to the interference with the SM contribution (see Eq. (14)).

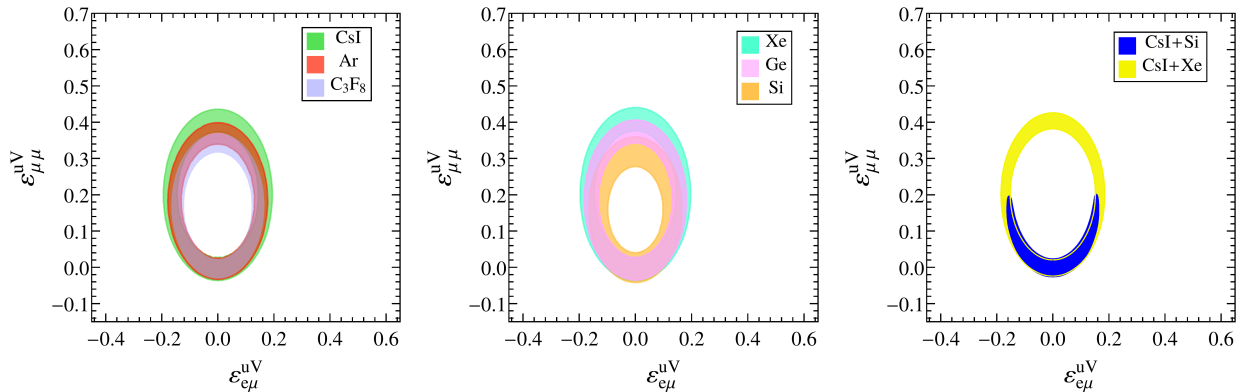


FIG. 9. Expected 90% C. L. sensitivities (with two d.o.f., i.e. $\Delta\chi^2 \leq 4.61$) in the $(\varepsilon_{e\mu}^{uV}, \varepsilon_{\mu\mu}^{uV})$ plane corresponding to different detectors or combination of detectors, assuming 3 years of data taking at the ESS for each detector. Left: CsI (green), Ar (red) and C_3F_8 (blue). Middle: Xe (cyan), Ge (magenta) and Si (orange). Right: combinations of detectors CsI + Xe (yellow) and CsI + Si (blue).

individual NSI parameters extracted from the COHERENT data. Then we quantified the further improvement that can be achieved when two detectors operate simultaneously. We found that the detector combination CsI + Si has one of the best sensitivities to the individual NSI parameters, and that the improvement with respect to a single target material is particularly significant for the flavor-diagonal parameters ε_{ee}^{uV} , $\varepsilon_{\mu\mu}^{dV}$ and especially $\varepsilon_{\mu\mu}^{uV}$. The combined analysis of the results of two detectors is an even more powerful tool when two NSI parameters are assumed to be nonvanishing at a time. We considered different detector combinations and studied their ability to partially break the degeneracies between two NSI parameters, for a large set of pairs of parameters. We found that the best choices are the ones that combine nuclei with a different proton to neutron ratio. In particular, we identified CsI + Si (together with CsI + C_3F_8 , Xe + C_3F_8 and Xe + Si) as one of the most efficient detector combinations, able to reduce the degeneracies between certain pairs of NSI parameters to a small region in the corresponding parameter space. Finally, we note that a longer running time than the one considered in this paper (3 years) would further improve the sensitivity of these combinations of detectors to NSI parameters, either taken individually or two at a time.

ACKNOWLEDGMENTS

S. S. C. acknowledges financial support from the LabEx P2IO (ANR-10-LABX-0038 - Project “BSM-Nu”) in the framework of the “Investissements d’Avenir” (ANR-11-IDEX-0003-01) managed by the Agence Nationale de la Recherche (ANR), France. The work of S. S. C. and S. L. is supported in part by the European Union’s Horizon 2020 research and innovation programme under the Marie Skłodowska-Curie grant agreement No. 860881-HIDDeN. The work of O. G. M. and G. S. G. has been supported in part by CONACYT-Mexico under grant A1-S-23238. O. G. M. has been supported by SNI (Sistema Nacional de Investigadores, Mexico). This work has been supported by the Spanish grants PID2020-113775GB-I00 (AEI/10.13039/501100011033) and CIPROM/2021/054 (Generalitat Valenciana).

-
- [1] D. Z. Freedman, “Coherent effects of a weak neutral current,” *Phys. Rev. D* **9** (Mar, 1974) 1389–1392. <https://link.aps.org/doi/10.1103/PhysRevD.9.1389>.
- [2] **COHERENT** Collaboration, D. Akimov et al., “The COHERENT Experiment at the Spallation Neutron Source,” [arXiv:1509.08702](https://arxiv.org/abs/1509.08702) [[physics.ins-det](#)].
- [3] **COHERENT** Collaboration, D. Akimov et al., “Observation of Coherent Elastic Neutrino-Nucleus Scattering,” *Science* **357** no. 6356, (2017) 1123–1126, [arXiv:1708.01294](https://arxiv.org/abs/1708.01294) [[nucl-ex](#)].
- [4] **COHERENT** Collaboration, D. Akimov et al., “First Measurement of Coherent Elastic Neutrino-Nucleus Scattering on Argon,” *Phys. Rev. Lett.* **126** no. 1, (2021) 012002, [arXiv:2003.10630](https://arxiv.org/abs/2003.10630) [[nucl-ex](#)].
- [5] D. Akimov et al., “Measurement of the Coherent Elastic Neutrino-Nucleus Scattering Cross Section on CsI by COHERENT,” [arXiv:2110.07730](https://arxiv.org/abs/2110.07730) [[hep-ex](#)].
- [6] D. K. Papoulias, “COHERENT constraints after the COHERENT-2020 quenching factor measurement,” *Phys. Rev. D* **102** no. 11, (2020) 113004, [arXiv:1907.11644](https://arxiv.org/abs/1907.11644) [[hep-ph](#)].
- [7] A. N. Khan and W. Rodejohann, “New physics from COHERENT data with an improved quenching factor,” *Phys. Rev. D* **100** no. 11, (2019) 113003, [arXiv:1907.12444](https://arxiv.org/abs/1907.12444) [[hep-ph](#)].
- [8] M. Cadeddu, F. Dordei, C. Giunti, Y. F. Li, and Y. Y. Zhang, “Neutrino, electroweak, and nuclear physics from COHERENT elastic neutrino-nucleus scattering with refined quenching factor,” *Phys. Rev. D* **101** no. 3, (2020) 033004, [arXiv:1908.06045](https://arxiv.org/abs/1908.06045) [[hep-ph](#)].
- [9] O. Miranda, D. Papoulias, G. Sanchez Garcia, O. Sanders, M. Tórtola, and J. Valle, “Implications of the first detection of coherent elastic neutrino-nucleus scattering (CEvNS) with Liquid Argon,” *JHEP* **05** (2020) 130, [arXiv:2003.12050](https://arxiv.org/abs/2003.12050) [[hep-ph](#)].
- [10] M. Cadeddu, N. Cargioli, F. Dordei, C. Giunti, Y. F. Li, E. Picciau, C. A. Ternes, and Y. Y. Zhang, “New insights into nuclear physics and weak mixing angle using electroweak probes,” *Phys. Rev. C* **104** no. 6, (2021) 065502, [arXiv:2102.06153](https://arxiv.org/abs/2102.06153) [[hep-ph](#)].
- [11] M. Cadeddu, C. Giunti, Y. Li, and Y. Zhang, “Average CsI neutron density distribution from COHERENT data,” *Phys. Rev. Lett.* **120** no. 7, (2018) 072501, [arXiv:1710.02730](https://arxiv.org/abs/1710.02730) [[hep-ph](#)].
- [12] B. C. Canas, E. A. Garces, O. G. Miranda, A. Parada, and G. Sanchez Garcia, “Interplay between nonstandard and nuclear constraints in coherent elastic neutrino-nucleus scattering experiments,” *Phys. Rev. D* **101** no. 3, (2020) 035012, [arXiv:1911.09831](https://arxiv.org/abs/1911.09831) [[hep-ph](#)].
- [13] P. Coloma, I. Esteban, M. C. Gonzalez-Garcia, and J. Menendez, “Determining the nuclear neutron distribution from Coherent Elastic neutrino-Nucleus Scattering: current results and future prospects,” *JHEP* **08** no. 08, (2020) 030, [arXiv:2006.08624](https://arxiv.org/abs/2006.08624) [[hep-ph](#)].
- [14] J. Barranco, O. G. Miranda, and T. I. Rashba, “Probing new physics with coherent neutrino scattering off nuclei,” *JHEP* **12** (2005) 021, [arXiv:hep-ph/0508299](https://arxiv.org/abs/hep-ph/0508299).
- [15] K. Scholberg, “Prospects for measuring coherent neutrino-nucleus elastic scattering at a stopped-pion neutrino source,” *Phys. Rev. D* **73** (2006) 033005, [arXiv:hep-ex/0511042](https://arxiv.org/abs/hep-ex/0511042).
- [16] J. Liao and D. Marfatia, “COHERENT constraints on nonstandard neutrino interactions,” *Phys. Lett. B* **775** (2017) 54–57, [arXiv:1708.04255](https://arxiv.org/abs/1708.04255) [[hep-ph](#)].
- [17] C. Giunti, “General COHERENT constraints on neutrino nonstandard interactions,” *Phys. Rev. D* **101** no. 3, (2020) 035039, [arXiv:1909.00466](https://arxiv.org/abs/1909.00466) [[hep-ph](#)].
- [18] P. B. Denton and J. Gehrlein, “A Statistical Analysis of the COHERENT Data and Applications to New Physics,” *JHEP* **04** (2021) 266, [arXiv:2008.06062](https://arxiv.org/abs/2008.06062) [[hep-ph](#)].
- [19] A. Galindo-Uribarri, O. G. Miranda, and G. S. Garcia, “Novel approach for the study of coherent elastic neutrino-nucleus scattering,” *Phys. Rev. D* **105** no. 3, (2022) 033001, [arXiv:2011.10230](https://arxiv.org/abs/2011.10230)

- [hep-ph].
- [20] A. N. Khan, D. W. McKay, and W. Rodejohann, “CP-violating and charged current neutrino nonstandard interactions in $CE\nu NS$,” *Phys. Rev. D* **104** no. 1, (2021) 015019, [arXiv:2104.00425 \[hep-ph\]](#).
- [21] B. Dutta, Y. Gao, R. Mahapatra, N. Mirabolfathi, L. E. Strigari, and J. W. Walker, “Sensitivity to oscillation with a sterile fourth generation neutrino from ultra-low threshold neutrino-nucleus coherent scattering,” *Phys. Rev. D* **94** no. 9, (2016) 093002, [arXiv:1511.02834 \[hep-ph\]](#).
- [22] M. Lindner, W. Rodejohann, and X.-J. Xu, “Coherent Neutrino-Nucleus Scattering and new Neutrino Interactions,” *JHEP* **03** (2017) 097, [arXiv:1612.04150 \[hep-ph\]](#).
- [23] D. Aristizabal Sierra, V. De Romeri, and N. Rojas, “COHERENT analysis of neutrino generalized interactions,” *Phys. Rev. D* **98** (2018) 075018, [arXiv:1806.07424 \[hep-ph\]](#).
- [24] L. J. Flores, N. Nath, and E. Peinado, “ $CE\nu NS$ as a probe of flavored generalized neutrino interactions,” *Phys. Rev. D* **105** no. 5, (2022) 055010, [arXiv:2112.05103 \[hep-ph\]](#).
- [25] Y. Farzan, M. Lindner, W. Rodejohann, and X.-J. Xu, “Probing neutrino coupling to a light scalar with coherent neutrino scattering,” *JHEP* **05** (2018) 066, [arXiv:1802.05171 \[hep-ph\]](#).
- [26] P. B. Denton, Y. Farzan, and I. M. Shoemaker, “Testing large non-standard neutrino interactions with arbitrary mediator mass after COHERENT data,” *JHEP* **07** (2018) 037, [arXiv:1804.03660 \[hep-ph\]](#).
- [27] L. J. Flores, N. Nath, and E. Peinado, “Non-standard neutrino interactions in $U(1)$ ’ model after COHERENT data,” *JHEP* **06** (2020) 045, [arXiv:2002.12342 \[hep-ph\]](#).
- [28] M. Cadeddu, N. Cargioli, F. Dordei, C. Giunti, Y. F. Li, E. Picciau, and Y. Y. Zhang, “Constraints on light vector mediators through coherent elastic neutrino nucleus scattering data from COHERENT,” *JHEP* **01** (2021) 116, [arXiv:2008.05022 \[hep-ph\]](#).
- [29] H. Banerjee, B. Dutta, and S. Roy, “Probing $L\mu-L\tau$ models with $CE\nu NS$: A new look at the combined COHERENT CsI and Ar data,” *Phys. Rev. D* **104** no. 1, (2021) 015015, [arXiv:2103.10196 \[hep-ph\]](#).
- [30] L. M. G. de la Vega, L. J. Flores, N. Nath, and E. Peinado, “Complementarity between dark matter direct searches and $CE\nu NS$ experiments in $U(1)$ ’ models,” *JHEP* **09** (2021) 146, [arXiv:2107.04037 \[hep-ph\]](#).
- [31] E. Bertuzzo, G. Grilli di Cortona, and L. M. D. Ramos, “Probing light vector mediators with coherent scattering at future facilities,” *JHEP* **06** (2022) 075, [arXiv:2112.04020 \[hep-ph\]](#).
- [32] J. Billard, J. Johnston, and B. J. Kavanagh, “Prospects for exploring New Physics in Coherent Elastic Neutrino-Nucleus Scattering,” *JCAP* **11** (2018) 016, [arXiv:1805.01798 \[hep-ph\]](#).
- [33] G. Arcadi, M. Lindner, J. Martins, and F. S. Queiroz, “New physics probes: Atomic parity violation, polarized electron scattering and neutrino-nucleus coherent scattering,” *Nucl. Phys. B* **959** (2020) 115158, [arXiv:1906.04755 \[hep-ph\]](#).
- [34] T. S. Kosmas, D. K. Papoulias, M. Tortola, and J. W. F. Valle, “Probing light sterile neutrino signatures at reactor and Spallation Neutron Source neutrino experiments,” *Phys. Rev. D* **96** no. 6, (2017) 063013, [arXiv:1703.00054 \[hep-ph\]](#).
- [35] O. G. Miranda, G. Sanchez Garcia, and O. Sanders, “Coherent elastic neutrino-nucleus scattering as a precision test for the Standard Model and beyond: the COHERENT proposal case,” *Adv. High Energy Phys.* **2019** (2019) 3902819, [arXiv:1902.09036 \[hep-ph\]](#).
- [36] O. G. Miranda, D. K. Papoulias, O. Sanders, M. Tórtola, and J. W. F. Valle, “Future $CE\nu NS$ experiments as probes of lepton unitarity and light-sterile neutrinos,” *Phys. Rev. D* **102** (2020) 113014, [arXiv:2008.02759 \[hep-ph\]](#).

- [37] A. N. Khan, “Extra dimensions with light and heavy neutral leptons: an application to $CE\nu NS$,” *JHEP* **01** (2023) 052, [arXiv:2208.09584 \[hep-ph\]](#).
- [38] M. Cadeddu, F. Dordei, C. Giunti, Y. F. Li, E. Picciau, and Y. Y. Zhang, “Physics results from the first COHERENT observation of coherent elastic neutrino-nucleus scattering in argon and their combination with cesium-iodide data,” *Phys. Rev. D* **102** no. 1, (2020) 015030, [arXiv:2005.01645 \[hep-ph\]](#).
- [39] O. G. Miranda, D. K. Papoulias, M. Tórtola, and J. W. F. Valle, “Probing neutrino transition magnetic moments with coherent elastic neutrino-nucleus scattering,” *JHEP* **07** (2019) 103, [arXiv:1905.03750 \[hep-ph\]](#).
- [40] D. Aristizabal Sierra, V. De Romeri, L. J. Flores, and D. K. Papoulias, “Impact of COHERENT measurements, cross section uncertainties and new interactions on the neutrino floor,” *JCAP* **01** no. 01, (2022) 055, [arXiv:2109.03247 \[hep-ph\]](#).
- [41] C. von Raesfeld and P. Huber, “Use of $CE\nu NS$ to monitor spent nuclear fuel,” *Phys. Rev. D* **105** no. 5, (2022) 056002, [arXiv:2111.15398 \[hep-ph\]](#).
- [42] **CCM** Collaboration, A. A. Aguilar-Arevalo *et al.*, “First Dark Matter Search Results From Coherent CAPTAIN-Mills,” [arXiv:2105.14020 \[hep-ex\]](#).
- [43] D. Baxter *et al.*, “Coherent Elastic Neutrino-Nucleus Scattering at the European Spallation Source,” *JHEP* **02** (2020) 123, [arXiv:1911.00762 \[physics.ins-det\]](#).
- [44] **CONUS** Collaboration, H. Bonet *et al.*, “Novel constraints on neutrino physics beyond the standard model from the CONUS experiment,” *JHEP* **05** (2022) 085, [arXiv:2110.02174 \[hep-ph\]](#).
- [45] **CONNIE** Collaboration, A. Aguilar-Arevalo *et al.*, “Results of the Engineering Run of the Coherent Neutrino Nucleus Interaction Experiment (CONNIE),” *JINST* **11** no. 07, (2016) P07024, [arXiv:1604.01343 \[physics.ins-det\]](#).
- [46] **NUCLEUS** Collaboration, G. Angloher *et al.*, “Exploring $CE\nu NS$ with NUCLEUS at the Chooz nuclear power plant,” *Eur. Phys. J. C* **79** no. 12, (2019) 1018, [arXiv:1905.10258 \[physics.ins-det\]](#).
- [47] J. Billard *et al.*, “Coherent Neutrino Scattering with Low Temperature Bolometers at Chooz Reactor Complex,” *J. Phys. G* **44** no. 10, (2017) 105101, [arXiv:1612.09035 \[physics.ins-det\]](#).
- [48] O. Tomalak, P. Machado, V. Pandey, and R. Plestid, “Flavor-dependent radiative corrections in coherent elastic neutrino-nucleus scattering,” *JHEP* **02** (2021) 097, [arXiv:2011.05960 \[hep-ph\]](#).
- [49] J. Erler and R. Ferro-Hernández, “Weak Mixing Angle in the Thomson Limit,” *JHEP* **03** (2018) 196, [arXiv:1712.09146 \[hep-ph\]](#).
- [50] **Particle Data Group** Collaboration, “Review of particle physics,” *Phys. Rev. D* **98** (Aug, 2018) 030001. <https://link.aps.org/doi/10.1103/PhysRevD.98.030001>.
- [51] R. H. Helm, “Inelastic and Elastic Scattering of 187-Mev Electrons from Selected Even-Even Nuclei,” *Phys. Rev.* **104** (1956) 1466–1475.
- [52] D. K. Papoulias, R. Sahu, T. S. Kosmas, V. K. B. Kota, and B. Nayak, “Novel neutrino-floor and dark matter searches with deformed shell model calculations,” *Adv. High Energy Phys.* **2018** (2018) 6031362, [arXiv:1804.11319 \[hep-ph\]](#).
- [53] D. K. Papoulias, T. S. Kosmas, R. Sahu, V. K. B. Kota, and M. Hota, “Constraining nuclear physics parameters with current and future COHERENT data,” *Phys. Lett. B* **800** (2020) 135133, [arXiv:1903.03722 \[hep-ph\]](#).
- [54] M. Hoferichter, J. Menéndez, and A. Schwenk, “Coherent elastic neutrino-nucleus scattering: EFT analysis and nuclear responses,” *Phys. Rev. D* **102** no. 7, (2020) 074018, [arXiv:2007.08529 \[hep-ph\]](#).

- [55] J. Friedrich and N. Voegler, “The salient features of charge density distributions of medium and heavy even-even nuclei determined from a systematic analysis of elastic electron scattering form factors,” [Nucl. Phys. A](#) **373** (1982) 192–224.
- [56] L. Wolfenstein, “Neutrino Oscillations in Matter,” [Phys.Rev.](#) **D17** (1978) 2369–2374.
- [57] I. Angeli and K. P. Marinova, “Table of experimental nuclear ground state charge radii: An update,” [Atom. Data Nucl. Data Tabl.](#) **99** no. 1, (2013) 69–95.
- [58] S. P. Mikheyev and A. Y. Smirnov, “Resonance Amplification of Oscillations in Matter and Spectroscopy of Solar Neutrinos,” [Sov. J. Nucl. Phys.](#) **42** (1985) 913–917.
- [59] O. G. Miranda, M. A. Tortola, and J. W. F. Valle, “Are solar neutrino oscillations robust?,” [JHEP](#) **10** (2006) 008, [arXiv:hep-ph/0406280](#).
- [60] P. Coloma and T. Schwetz, “Generalized mass ordering degeneracy in neutrino oscillation experiments,” [Phys. Rev. D](#) **94** no. 5, (2016) 055005, [arXiv:1604.05772 \[hep-ph\]](#). [Erratum: [Phys.Rev.D](#) 95, 079903 (2017)].
- [61] I. Esteban, M. C. Gonzalez-Garcia, M. Maltoni, I. Martinez-Soler, and J. Salvado, “Updated constraints on non-standard interactions from global analysis of oscillation data,” [JHEP](#) **08** (2018) 180, [arXiv:1805.04530 \[hep-ph\]](#). [Addendum: [JHEP](#) 12, 152 (2020)].
- [62] P. Coloma, I. Esteban, M. C. Gonzalez-Garcia, and M. Maltoni, “Improved global fit to Non-Standard neutrino Interactions using COHERENT energy and timing data,” [JHEP](#) **02** (2020) 023, [arXiv:1911.09109 \[hep-ph\]](#). [Addendum: [JHEP](#) 12, 071 (2020)].
- [63] M. Chaves and T. Schwetz, “Resolving the LMA-dark NSI degeneracy with coherent neutrino-nucleus scattering,” [JHEP](#) **05** (2021) 042, [arXiv:2102.11981 \[hep-ph\]](#).